Supplementary Information:

Lithium permeation within lithium niobate multilayers with ultrathin chromium, silicon and carbon spacer layers

Erwin Hüger[1,*], Lars Dörrer[1], R. Yimnirun[2], J. Jutimoosik[3] and Jochen Stahn[4] and Amitesh Paul[5]

[1]Institute of Metallurgy, Microkinetics Group, Clausthal University of Technology, Robert-Koch-Str. 42, D-38678 Clausthal Zellerfeld,
Germany
[2]School of Energy Science and Engineering, Vidyasirimedhi Institute of Science and Technology,
Wang Chan Valley, Rayong 21210,
Thailand
[3]Department of Physics, Faculty of Science, Naresuan University, Phitsanulok, 65000,
Thailand
[4]Laboratory for Neutron Scattering and Imaging, Paul-Scherrer-Institut, CH-5232 Villigen PSI,
Switzerland
[5]Technische Universität München, Physik Department E21, Lehrstuhl für Neutronenstreuung,
James-Franck-Straße 1, D-85748 Garching,
Germany

*Corresponding author
e-mail: erwin.hueger@tu-clausthal.de

Content

The supplemental material possesses details and additional material about

1. Literature survey

This section provides a literature survey on the academic and technological interest for laminar structures of alternating ultrathin layers of amorphous $LiNbO_3$ and spacer layers of other materials (e.g. Cr) (superlattices [1]) which enable the measurement of Li permeation through thin spacer (e.g. Cr) layers and interfaces.

$LiNbO_3$ is a perovskite. Materials with such structure turn nowadays to be on the research focus to develop more efficient energy materials [11-22], e.g. non-oxide perovskite solar cells [19-22] and oxide based perovskites for photovoltaics [14,15]. There is an intensified research on perovskites oxides (ABO_3) for increasing recoverable energy storage in electroceramic capacitors [23-26] and for lowering the operation temperature in (i) fuel cells [11,12] and (ii) solar thermo-chemical syngas (e.g. H_2 and CO) production [19-22]. Layered materials of oxide perovskite / metal (multilayers) [25] are investigated to achieve environmentally friendly solid state refrigeration free of greenhouse gases [25,26] and to recover useful electrical power from waste heat [24].

From the class of perovskites, $LiNbO_3$ is one of the most technologically important material in science and technology due to its favourable combination of pyroelectric, piezoelectric, electrocaloric, acousto-optical, giant-photovoltaic, ferro-electric, electro-optical, photorefractive and non-linear optical properties [27-32] and not at least due to energy conversion properties [21,33-60] combined with an easy fabrication technique and low fabrication costs [27,61]. Moreover, Li mobility in $LiNbO_3$ plays, in general, a crucial role for a successfully implementation of the versatile properties of $LiNbO_3$ in the performance of $LiNbO_3$ based devices [62]. Mesoporous, nano-crystalline [33-43,63] and amorphous [44,64,65] films of $LiNbO_3$ are of special interest in development of advanced electrochemical energy storage devices. It was found that the amorphous state of $LiNbO_3$ [44,53-56,63] possess a high Li conductivity, a prerequisite for proper charge storage (battery) operation. Consequently, $LiNbO_3$, possessing a high density of defects (as they are present in the amorphous state), is an material also for use in electrical devices which depend on Li ionic motion [33-51,53,63-67]. Accordingly, Li-Nb-O compounds (ranging from $LiNbO_3$ [34-37,44-46,50-53,63-66] over $LiNb_3O_8$ [34,35,38,39], to niobium oxides (e.g. Nb_2O_5) [40-43,60,67]) were used as part of solid electrolyte for Li ion batteries [40,41,44,46,47,49-53,64,65] and for electro-chromic devices [44-46,48,49]. They were used also in electrodes as an active material for Li ion batteries [33-43,60,68] and electrochromic devices [67]. Nanoparticles of lithium oxides embedded in a cage of cobalt oxide, which network is similar to that of lithium oxides in niobium oxides, could overcome key drawbacks of lithium-air batteries [69]. $LiNbO_3$ in the form of thin films is of special interest to improve the operation of lithium ion batteries by reducing the space charge layer barrier for Li motion on electrolyte / electrode interfaces [64-66]. Interface engineering in energy conversion cells based on perovskite thin layers [13,17,21] is of special research due to charge carriers effects [13,17].

Interfaces, stresses and atomic transport (defect kinetics) which exists in superlattices can change the magnetic property of layers. For example, interfaces, layer thicknesses (quantum size effects [70]), stresses and atomic transport can change the lattice structure and the impurity (e.g. lithium and/or oxygen) concentration, which can induce ferromagnetism in native non-ferromagnetic materials [71-76]. For such investigations chromium is of special interest. Elemental chromium is a metallic anti-ferromagnet. A changed structure [72-76] or a changed chemical composition would turn anti-ferromagnetic order into a ferromagnetic spin alignment. In general, the oxidation of metals reduces the density of states at the Fermi energy and, in this way it should inhibit a possible ferromagnetic ordering [72-76] in chromium. In contrary, this is not the case for oxidised chromium, where higher oxygen content induces ferromagnetic order. Chromia (Cr_2O_3), the most stable chromium oxide, is an antiferromagnetic insulator with excellent dielectric properties for attempts to utilize this material as a "gate" dielectric in future spintronic devices [77,78]. Chromium monoxide CrO does not exist as a bulk material, but can be grown on cubic substrates as Cr_xO ($0.67<x<1$). Higher oxygen content induces a ferromagnetic spin alignment. Chromium dioxide (CrO_2) films grown by high-pressure thermal decomposition of CrO_3 is a ferromagnetic ordered half-metal [79]. The Neel temperature can be tuned by alloying the antiferromagnetic insulator Cr_2O_3 with other metal oxides [80]. So, rich changes can be expected to appear in Cr / $LiNbO_3$ multilayers, by the interplay of layer thicknesses, interfaces, stresses and atomic transport. It is anticipated that heat treatments will change the (i) stress level, (ii) lithium and (iii) oxygen content by atomic transport inside the Cr spacer layers and (iv) Schottky contact on the interface. All this points can drive the superlattice into different properties.

Regarding the stress level in superlattices, one may note that electric fields can appear if the superlattices possess layers of piezoelectric material (e.g. $LiNbO_3$). If these layers are under strain a piezoelectric electric field over the (e.g. Cr) spacer layer can appear which can promote or suppress Li ion transport [138,139]. This is of importance for self-charging LIB that hybridize mechanical energy harvesting and ion storage processes into one process [138,139]. The electric field can affect also the electronic structure of the spacer layer and change the property of the superlattice.

Further, it is worth mentioning that Cr is often used as an adhesion layer in several applications [81,82]. Traditional silicon processing methods use a chromium adhesion layer. Up to 50 nm thin Cr layers are used as drain material in the fabrication of metal oxide semiconductor thin-film transistors for flexible electronics [83,84]. The thin Cr layer is used for top gate contact due to its adhesion properties, suitability for the wet etching processes and low water permeation characteristics [83]. Thinner (10 to 22 nm thin) Cr adhesion layers are used for building flexible fluidic sensing [85] and energy [86] devices.

Regarding the change of chemical bonds let mention that superlattices build up by alternating Cr and oxide layers (such as $LiNbO_3$) can produce thin $LiCrO_2$ layers on interfaces. On the one hand, the thin fashion of the layers would enhance electrochemical lithium storage activity [87]. On the other hand, a common origin for inactivity of some cathode materials is a surface blocking phenomena of cations conglomerates against Li migration. It was found that the irreversible migration of Cr into Li layers increases the diffusion energy barrier of Li ions [88]. Some information about the appeared energy barrier for Li motion can be investigated by Li permeation experiments through thin Cr sheets.

Recently we introduced multilayers which combines amorphous $LiNbO_3$ layers with Si spacer layers (i.e. [$LiNbO_3$ / Si] multilayers) to measure Li permeation trough Si layers [89]. In this work we add-on to this new class of multilayers $LiNbO_3$ layers spaced by ultrathin Cr and C layers. The work reports besides the superlattice fabrication and characterization, although about Li permeation experiments through ultrathin Si, Cr and C layers, respectively. The aim of the Li permeation experiments is to compare the ability of ultrathin Si, Cr and C layers to conduct Li.

2. Multilayer preparation and applied experimental techniques

Multilayer films as sketched in Fig.S1 were deposited using an ion-beam coater (IBC 681) delivered by Gatan, Inc. (Pleasanton, CA, USA). Sputtering is accomplished by two miniature Penning ion guns at a glancing angle of 45 °, positioned about 10 cm above the sample. Different target materials can be selected without breaking the vacuum. The $^{6}LiNbO_3$ and $^{nat}LiNbO_3$ sputter targets were prepared by solid state syntheses as described in Ref. [55]. The Si sputter target was purchased from Alfa Aesar (99.999%). The Cr and C sputter target was delivered by Gatan Inc. (Pleasanton, CA, USA). The base pressure of the vacuum chamber was 5 x 10^{-7} mbar. Sputtering was done with Ar^+ ions at a working pressure of 5 x 10^{-5} mbar. The ion beam acceleration voltage was 5 kV and the ion beam current was 180 µA. During deposition, the specimen is rotated (30 rotations per minute) and rocked (rock angle: 30° and rock speed: 12° per second) to ensure a more uniform coating of the sample. The deposition rate was determined non-destructively by X-ray reflectometry (XRR) by analysing Kiesig fringes [90,91]. Multilayer deposition was done on 650 µm thick (100) oriented silicon wafers. Prior to multilayer deposition, each target was pre-sputtered for 15 minutes to remove a possible contaminated surface layer. After deposition of a desired layer, deposition was interrupted by introducing a shutter between the sputter target and the sample. Now, the next target was brought into the sputtering position and was again pre-sputtered for 30 s (with the shutter closed). Afterwards the ion beam current was manually re-adjusted to a value of 180 µA, and deposition of the next layer was done. The depositions were performed at room temperature.

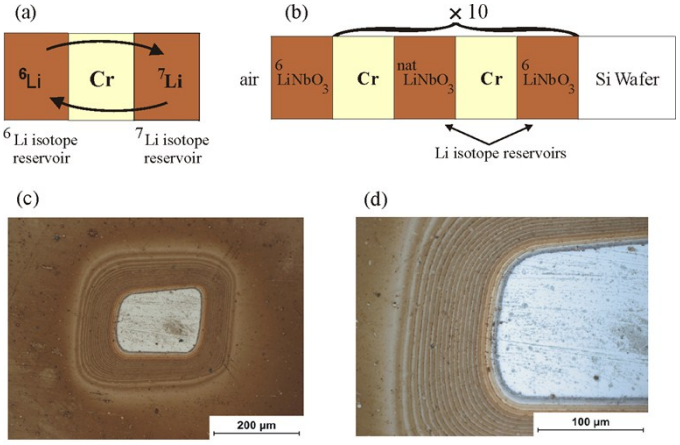

Figure S1: (a) Basic principle of the experimental arrangement: two Li isotope reservoir layers are spaced by a Cr (or Si) layer. **(b)** Sketch of the multilayer produced for the NR measurements. **(c,d)** Light microscopy for visualization of the multilayer arrangement. Micrographs of a crater obtained by SIMS depth profiling of multilayer system composed by 8 nm thin Cr layers embedded between 9 nm thin $LiNbO_3$ layers. The crater bottom (silicon wafer) is the white region in the middle. The rings located at the crater edge correspond to the $LiNbO_3$/Cr multilayer structure.

Neutron reflectometry is a non-destructive technique which is sensitive on Li isotopes because ^{6}Li has a strongly different neutron scattering length (i.e. a positive value of 2.00 + i 0.261 fm) in comparison to ^{7}Li (i.e. a negative value of −2.22 fm). NR was applied to measure, both, i.e. the chemical and isotope contrast in the multilayer. The measurements were performed at the reflectometer AMOR and Morpheus located at SINQ, PSI Villigen, Switzerland. The samples used for NR had sizes of 10 x 10 x 0.65 mm^3. The NR curves at AMOR were recorded in the time-of-flight mode. The NR pattern recorded at Morpheus were in the θ/2θ mode in 0.005° or 0.01° angle steps using a neutron wavelength of 0.5 nm. During NR experiments the reflection of a beam of neutrons at surfaces and interfaces of an arrangement of thin layers (multilayer) and its mutual interference are measured. Single layer thicknesses, mass densities and the relative ^{6}Li and ^{7}Li fractions were determined by simulating the measured NR patterns with

the Parratt32 software package (based on Parratt's recursion algorithm) [92] and the scattering length density online calculator given in Ref. [93]. The Parratt32 code [92] is based on multiply reflection at layered structures. For NR simulations, a constant background of 2 x 10^{-5}, a constant resolution of 0.0005 $Å^{-1}$ at $Q_z = 0$ and a wave length resolution of $d\lambda/\lambda = 2$ % was used. Error limits correspond to a 10% increase of χ^2 of best fit with respect to the fitted parameter only [94].

Secondary ion mass spectrometry (SIMS) measurements were done using a CAMECA IMS-3F/4F machine with a double focused mass spectrometer and O_2^+ (5 keV, ~ 10 nA), Ar^+ (5 keV, ~ 10 nA) or O^- (15 keV, ~ 10 nA) primary ion beams. Positive secondary ions were recorded. Lithium has a high ionization cross section for positive ions. Hence, the Li^+ SIMS signal is of splendorous high intensity. The measured Li isotope SIMS signals were usually up to 1 million counts per second. From the sputtered area of about 250 µm × 250 µm, the signal resulting from an area of 60 µm × 60 µm in the centre was used for further processing in order to exclude crater edge effects. The measurements were performed at room temperature. Micrographs of SIMS craters were performed with a ZEISS AXIO ImagerM2m light microscope.

X-ray reflectometry (XRR) was used to determine the film thickness and to check the chemical contrast in the deposited multilayers. The in-house XRR technique was used to determine primarily the layer deposition rates. The amorphous or crystalline structure of the multilayer was confirmed with grazing incidence X-ray diffraction (GI-XRD) measurements. The X-ray measurements were performed with a Bruker D5000 diffractometer using a Co target for generation of X-ray radiation and a scintillation counter detector with soller slits.

Fourier transform infrared spectroscopy (FTIR) was performed in vacuum with a Bruker VERTEX 70V using a reflection geometry. Raman scattering were performed with a Bruker SENTERRA Raman microscope using a laser of 532 nm wavelength.

Magnetisation curves were measured using a superconducting quantum interference device (SQUID) from Quantum Design (MPMS-XL).

The Cr *K*-edge X-ray absorption fine structure **(**XAFS**)** measurements were performed in the fluorescent mode with a four-element Si drift detector at the X-ray absorption spectroscopy beamline (BL-5) of the Siam Photon Source (electron energy of 1.2 GeV, beam current 120–80 mA), Synchrotron Light Research Institute, Thailand. A double crystal monochromator Ge (220) was used to scan the energy of the synchrotron x-ray beam with energy steps of 0.30 eV.

3. Microscopy

Figure S-1a sketch the basic structure used for the investigations of Li transport through thin (Cr, Si or C) spacer layers. The multilayer sketched in Fig. S1b with twenty ($LiNbO_3$/spacer-layer) double layers was used for NR experiments.

The multilayer stack is visualized in Fig. S1c,d by surface micrographs of craters obtained after SIMS depth profiling. Rings are observed around (at the edge of) SIMS depth profile craters. The rings appear due to interplay of flat (oblique) SIMS crater edge and the layered periodical arrangement of the multilayer. The SIMS craters as visualized in Fig. S1 were obtained with a more defocussed SIMS primary ion (sputtering) beam. Such primary ion beams produce craters with long edges at low angle. The long flat edge cuts the multilayer with a low slope (oblique). Due to the grazing incidence of the crater edge, the cutting of each 10 nm thin layer is performed over several µm large distances. The top view optical micrograph (Fig.S1c,d) visualizes the material contrast of exactly this µm sized cutting edges of the individual (less than 10 nm thin) layers in the multilayer. The cutting edges appear as rings around the crater. In optical micrograph the rings appear as material bands with lateral sizes of some microns although the bands appear from the oblique cutting of less than 10 nm thin layers. Interestingly, the methodology (of top view light microscopy of craters obtained by depth profiling) enables the practical visualization of multilayer arrangement (with less than 10 nm thin individual layers) with only optical microscopy. Electron microscopy is not necessary to visualize the multilayer arrangement. However, in order to detect Li isotopes we performed depth profiling by SIMS and NR measurements.

4. Secondary Ion Mass Spectrometry

Figures S2 to S10 visualize the ^6Li / ^7Li isotope contrast existent in the $LiNbO_3$ layers of the multilayer with Si (Figs. S2,4,6,8), Cr (Figs. S3,5,7,8,9) and carbon (Fig. S10) spacer layers as obtained by SIMS depth profiling.

Figures S2 and S3 presents the SIMS depth profiles for the as-deposited multilayer with Si (Fig. S2) and Cr (Fig. S3) spacer layers. Astound periodically SIMS signals were measured in the depth profile with the (old) Cameca 3f equipment. The recorded Li^+ SIMS signals are extremely strong. Double peaked signals of Li isotopes and Cr masses were measured from the superlattice with Cr spacer layers. They are present for the superlattice with Cr spacer layers but absent for the multilayer with Si spacer layers. The double peaked SIMS signals persist also five years storage of the superlattices in air and room temperature (Fig. S5) and withstand even the annealing of the superlattice at 100°C for 11 hours (Figs. S7 and S8).

The ^{6}Li (and ^{7}Li) isotope ratios can be obtained from the SIMS signals by the following quotient of SIMS intensities

$$\chi_{6Li} = \frac{I_{SIMS}^{6Li}}{I_{SIMS}^{6Li} + I_{SIMS}^{7Li}} \quad ; \quad \chi_{7Li} = \frac{I_{SIMS}^{7Li}}{I_{SIMS}^{6Li} + I_{SIMS}^{7Li}} \qquad (S1)$$

where I_{SIMS}^{6Li} and I_{SIMS}^{7Li} are the SIMS intensities measured for the ^{6}Li and ^{7}Li masses.

The obtained Li isotope ratios are presented in the panels (d) and (e) of Figs. S2 to S7. Grand ^{6}Li / ^{7}Li isotope contrast is measured by SIMS in the as-deposited multilayers. The measured double peaked signals (panels (a,b) of Figs. S3,5,7 and panels (c-f) of Fig.S8) have no influence on the Li isotope fractions (panels (d) and (e) of Figs. S3, S5 and S7, and panel (i,j,k,l) of Figure S8).

Notice that the annealing procedure (Figure S8e,k,l,r,s) does not smooth the total (i.e., 6Li+7Li) Li content over the layers of the multilayers (Figure S8e,r,s). Annealing changes only the fraction of Li isotopes in the $LiNbO_3$ layer (Figure S8k,l, obtained by equation (S1)) without to change the Li content in the corresponding layer. Annealing leads to a mutual exchange of the two Li isotopes through the Si layer and adjacent interfaces without changing chemical compositions in the multilayer. Within this process the Li isotope fractions in the solid-state Li reservoirs are balanced. The total Li content in the Li reservoir layers is high, and the total Li content in the spacer layers (Si or Cr) is extremely low (Li solubility of less than one Li atom per million Si or Cr atoms, see the discussion and values given in the main work). The total Li content in the Li reservoir ($LiNbO_3$) layers (before annealing Figure S8c,o,p) remain unchanged after annealing (Figure S8e,r,s), and the Li content in the spacer layers (Si or Cr) remains low. As mentioned, only the Li isotope fraction is smoothed after annealing (compare Figure S8e with S8k,l). After Li isotope intermixing, only the Li isotope fractions are equally distributed over all the ML (in that case the Li isotope fractions are the same in the 6Li and 7Li reservoir, see Figure S8k,l). The Li content in the Li reservoir layer remains high and that in the spacer layer low.

The question arises if the double peaked signal arises from an intrinsically property of the multilayer or it is produced by the SIMS measurement themselves. In the latter case, the SIMS depth profile would not correspond to the real element distribution in the multilayer. This is a reasonable doubt due to the destructive manner of the SIMS measurement technique. For example, the sputter process with charge beams (ion beams) can produce pyroelectric effects in lithium niobate which has influences on the emitted and detected secondary ions. Figure S9 illustrates profoundly how the destructive manner of SIMS affects measured signals.

The SIMS signals presented in Fig. S9 were collected from an as-deposited superlattice with Cr spacer layers by using higher primary ion beam energy (Figure S9a,b,c,d) and by using different ion species for primary ion beam generation (Figure 9e,f,g,h). The depth profiles of Fig.S9 are different to those presented in Fig.S3, although the same sample was used for both SIMS measurements.

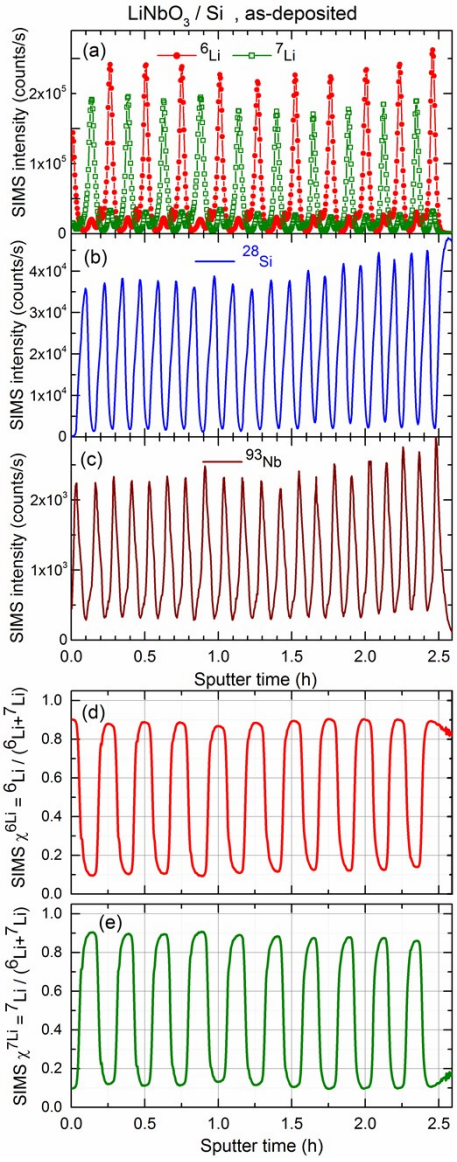

Figure S2: SIMS depth profiles of **(a)** Li isotopes, **(b)** ^{28}Si and **(c)** ^{93}Nb masses of the multilayer system with Si spacer layers in the as-deposited state after 5 days of storage in air at room temperature. Relative ^{6}Li **(d)** and ^{7}Li **(e)** fraction as obtained from the SIMS signals presented in panel (a) using eq. (1). (5 keV, O_2^+) primary ion beam.

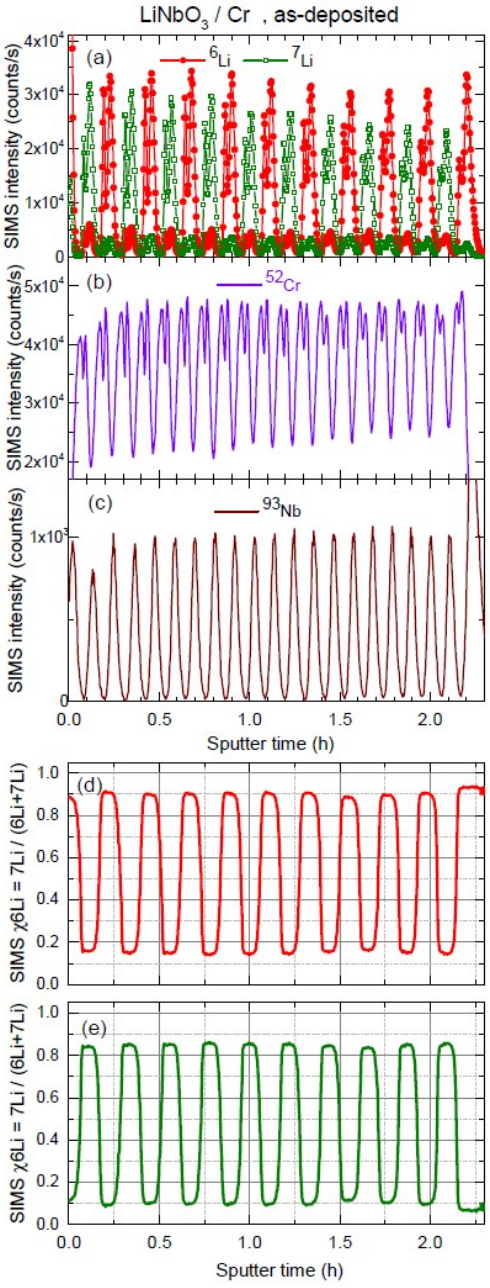

Figure S3: SIMS depth profiles of **(a)** Li isotopes, **(b)** ^{52}Cr and **(c)** ^{93}Nb masses of the superlattice with Cr spacer layers in the as-deposited state after 5 days of storage in air at room temperature. Relative ^{6}Li **(d)** and ^{7}Li **(e)** fraction as obtained from the SIMS signals presented in panel (a) using eq. (1). (5 keV, O_2^+) primary ion beam.

The sputter process with higher primary ion beam energy and with different ion species strongly changes the SIMS depth profiles. Also the Li isotope fractions are strongly changed, i.e. diminished (compare Fig.S3c,d with Fig.S9c,d,g,h). So, the SIMS measurement itself deteriorates the isotope and chemical contrast existent in the superlattice. From numerous SIMS experiments we argue that the depth profile obtained by SIMS is more close to the real one of the superlattice if SIMS is performed with primary ion beams possessing beside the lower kinetic energy of 5 keV (Fig.S3 compared to 15 keV in Fig.S9a,b,c,d) also larger ionic species (O_2^+ in Fig.S3 compared to (O^- and Ar^+) in Fig.S9).

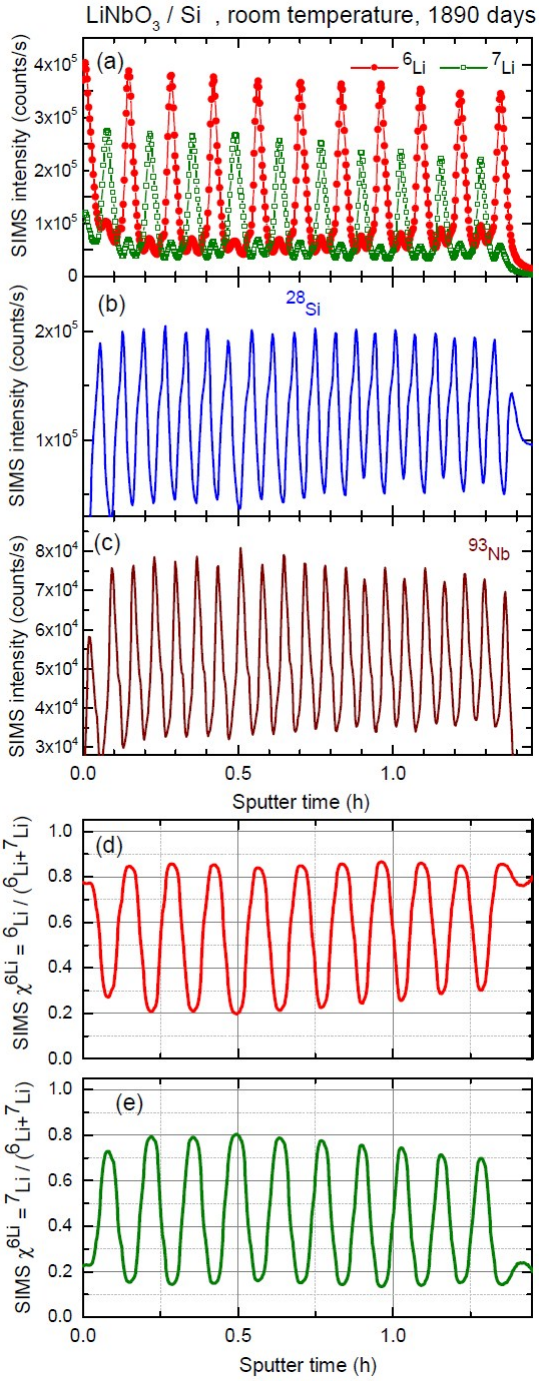

Figure S4: The same as Fig. S3 (multilayer with Si spacer layers), but measured after 1890 days of storage in air at room temperature. (5 keV, O_2^+) primary ion beam.

The influence of the storage in air at room temperature for above 5 years for the multilayer with Si spacer layers and for up to 5 years for the superlattice with Cr spacer layers is presented in Fig. S4 and Fig. S5, respectively. The Li isotope contrast is only marginally reduced (compare the panels (d,e) of Figs. S4,5 with those of Figs. S2,3).

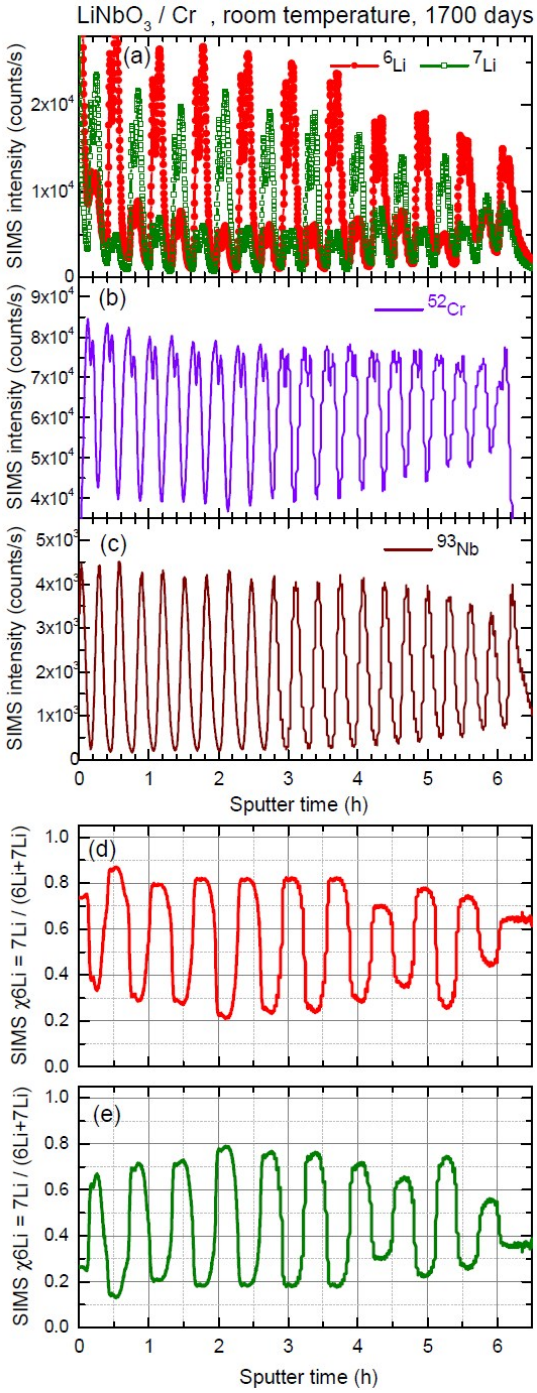

Figure S5: The same as Fig. S4 (superlattice with Cr spacer layers), but measured after 1700 days of storage in air at room temperature. (5 keV, O_2^+) primary ion beam.

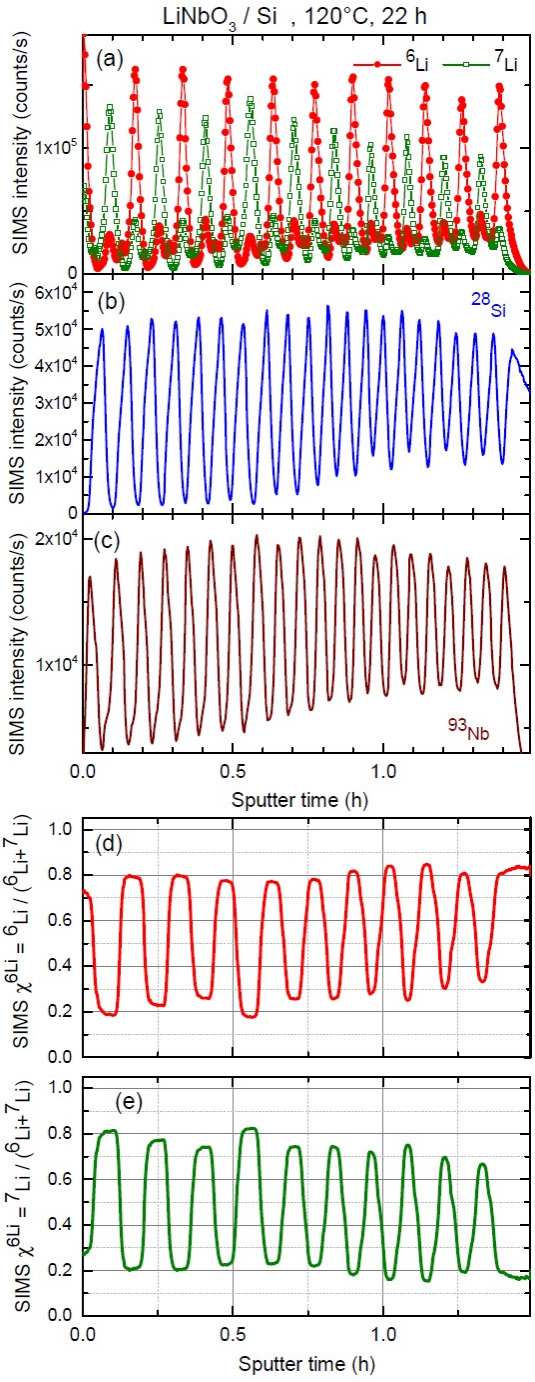

Figure S6: The same as Fig. S3 (multilayer with Si spacer layers), but measured after annealing at 120 °C for 22 hours. (5 keV, O_2^+) primary ion beam.

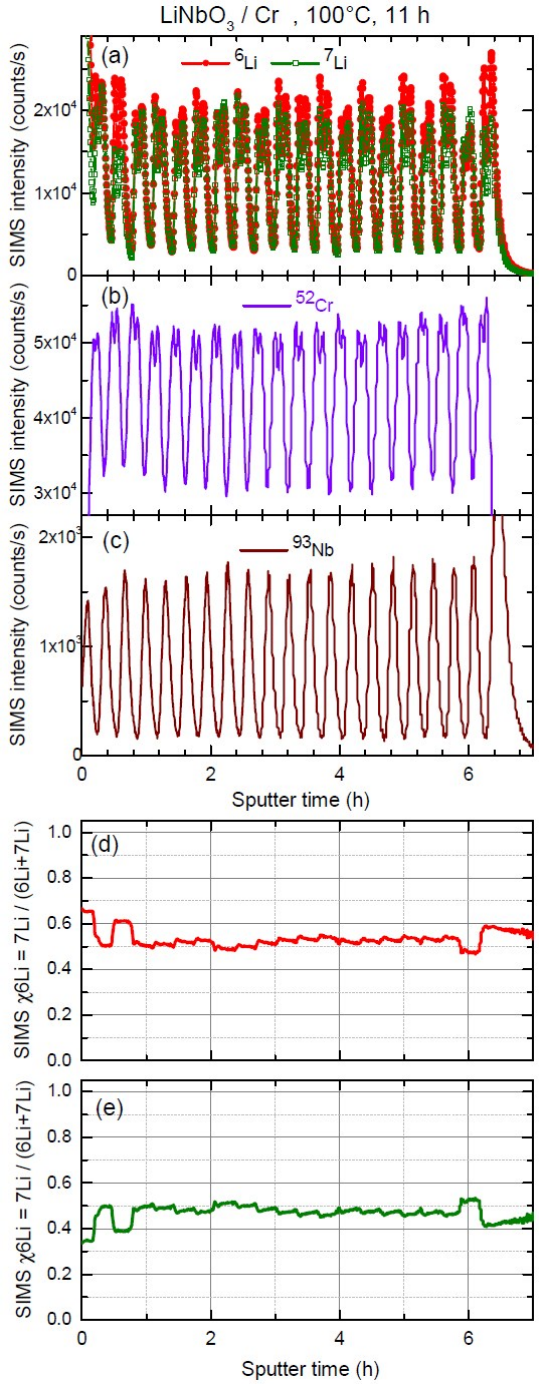

Figure S7: The same as Fig. S4 (superlattice with Cr spacer layers), but measured after annealing at 100 °C for 11 hours. (5 keV, O_2^+) primary ion beam.

Before presenting the annealing experiments, let mention the necessity of non-destructive methods for Li permeation measurement.

Figure S9 shows that even the SIMS measurement with low kinetic energy and large ionic species is risky for the demand to obtain reproducible results. A strangling (damping) of the SIMS signal appears in the last halve of the SIMS depth profile of Fig. S5. The depth profile strangling appears due to lack of a primary ion mass filter of the Cameca 3f machine. The O_2^+ primary ion beam is actually a mixture of molecular ions O_2^+ and 'atomic' ions O^+. It can be argued that the O^+ species in the primary ion beam produces the strangling effect in the depth profiling due to forward mixing in SIMS.

In generation and adjustment operations of the O_2^+ primary ion beam one is aimed to reduce as possible the percentage of O^+ ions in the primary ion beam. Unfortunately, the percentage of O^+ ions in the primary beam differs from one to the other primary ion beam generation and adjustment operation. Therefore, to be sure that the realistic Li isotope contrast is measured in the multilayer we choose to apply non-destructive methods to determine the Li isotope contrast for Li permeation determination and for further extended investigation of the multilayers characteristics.

The main purpose of the presented SIMS data with different ion beams (i.e. (5 kV, O_2^+), (5 kV, Ar^+), (15 kV, O^-) (Figure S9 and S10 of SI) was to show the destructive nature of sputter depth profiling on the ML network possessing ultrathin layers.

Nevertheless, there is a difference in the degradation of the Li isotope fraction. The main difference presented in Figure S9 and S10 is that there is a slight variation of Li isotope concentration with 15 kV O^- and high (more realistic) initial fluctuation with 5kV Ar in the beginning and strong degradation with sputtering time. The specimen was not rotated during SIMS measurements. The reason of the degradation is not absolutely clear. One reason might be the impact of the ion beam on the sample surface. This succeeds in more grazing incidence for positive than for negative ion beams. Another reason might be space charge layers inside the ML network. We hope that future resistivity measurements would help in elucidating this issue.

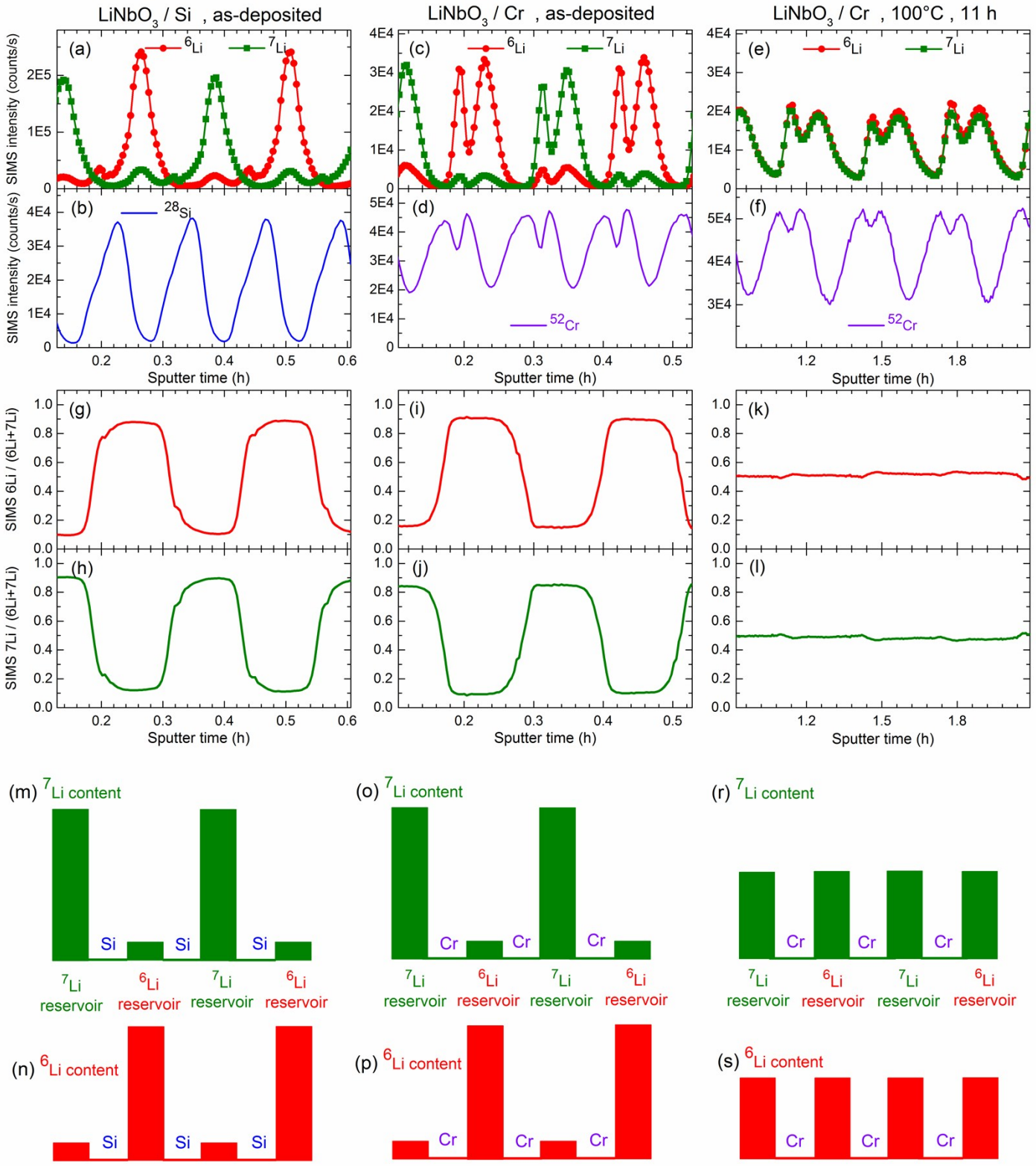

Figure S8: (a-f) Data of Figs. S2,3,7 on an enlarged scale for better visualisation of the peak splitting observed in the SIMS depth profiles of superlattice spaced by Cr layers. Depictured are SIMS signals from **(a,c,e)** Li isotopes, **(b)** ^{28}Si and **(d,f)** ^{52}Cr masses. (5 keV, O_2^+) primary ion beam. (**g-l**) 6Li (**g,i,k**) and 7Li (**h,j,l**) isotope fractions as determined from the 6li and 7Li SIMS signals presented in panel (**a,c,d**), respectively. (**m-s**) Sketches of 6Li (**n,p,s**) and 7Li (**m,o,r**) content in the as deposited ML with Si spacer layers (**m,n**), superlattice with Cr spacer layers (**o,p,r,s**) in the as-deposited state (**o,p**) and after annealing at 100°C (373K) for 11 hours (**r,s**). The Li content in the spacer layers (Si or Cr) is extremely low. The (total) Li content (i.e. 6Li+7Li) in the Li reservoir ($LiNbO_3$) layers (**c,o,p**) does not change after annealing (**e,r,s**). Only the Li isotope fraction in the Li reservoir layers (**i,j**) is smoothed after annealing (**k,l**). After annealing, the Li content in the Li reservoir ($LiNbO_3$) layers remains high and that in the spacer layers remains low.

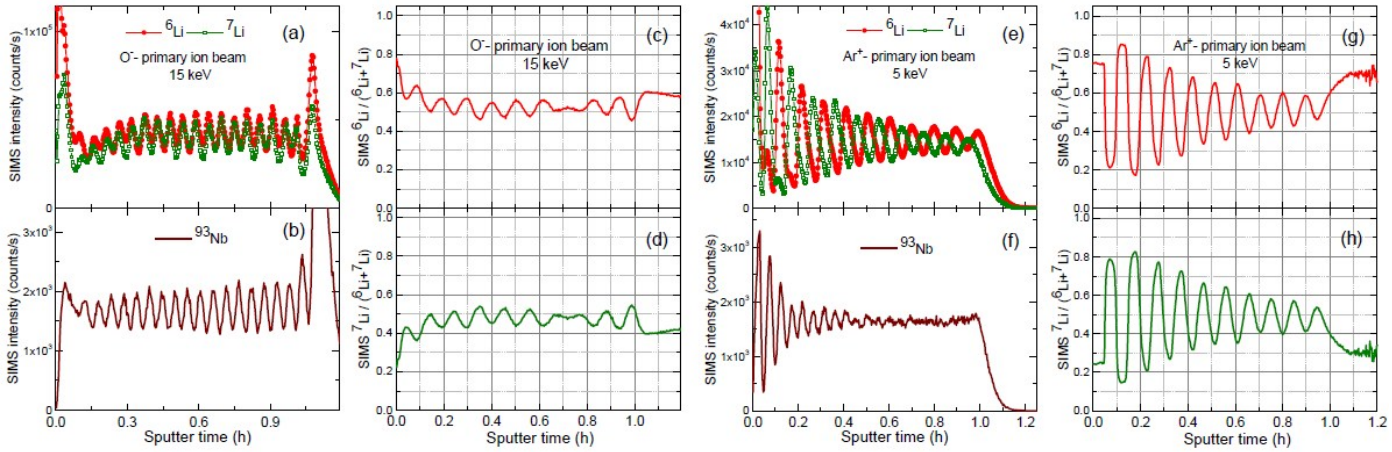

Figure S9: (a,b,e,f) SIMS depth profiles of **(a,e)** Li isotopes and **(b,f)** ^{93}Nb masses measured from the superlattice with Cr spacer layers recorded with O^- (a,b) and Ar^+ (e,f) primary ion beams. **(c,d,g,h)** Relative ^{6}Li (c,g) and ^{7}Li (d,h) fraction as obtained from the SIMS signals presented in panel (a) and (e), respectively. (**a-d**) (15 keV, O^-) and (**e-h**) (5 keV, Ar^+) primary ion beam.

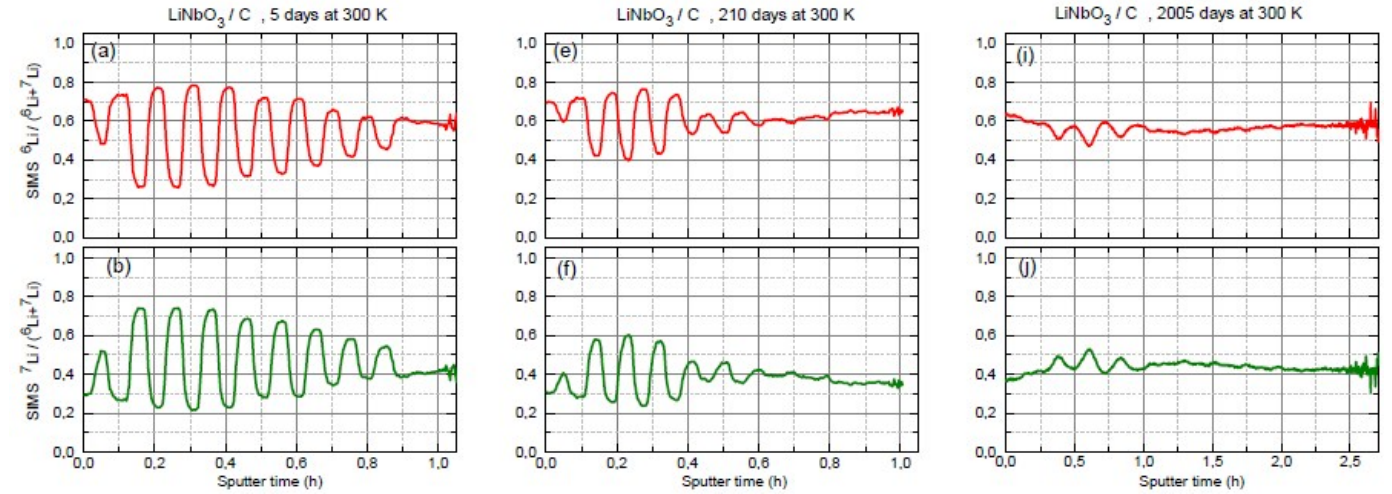

Figure S10: ^{6,7}Li isotope fraction in lithium niobate multilayers with carbon spacer layers as determined by SIMS depth profiles after 5 days **(a,b)** 210 days **(c,d)** and 2005 days **(e,f)** of ML storage in air and at room temperature. (5 keV, O_2^+) primary ion beam.

Figure S10 presents the Li isotope fraction in the multilayer with carbon spacer layers during ML storage at air and room temperature for more than five years. The Li isotope contrast of the $^6LiNbO_3$ layers was calculated as follows

$$K(t) = \frac{\chi(t) - \chi_{min}}{\chi_{max} - \chi_{min}} = \frac{\chi(t) - \chi(t \to \infty)}{\chi(t=0) - \chi(t \to \infty)} = \exp\left[-\frac{t}{\tau}\right] \qquad (2)$$

where χ is the Li isotope contrast.

The Li isotope contrast after full intermixing amounts to χ_{min} = 54 % because the the as deposited multilayer possess 11 $^6LiNbO_3$ layers with 96 % ^{6}Li isotope enrichment and 10 $^{nat}LiNbO_3$ layers which possess a 7.5 % ^{6}Li isotope fraction

$$\chi\,\min = \chi(t \to \infty) = \frac{11 \cdot 96\,\% + 10 \cdot 7.5\,\%}{21} \approx 54\% \qquad (3)$$

As an approximation χ_{max} = χ(t = 5 days) was used. According to eq. (2) and (3) the ^{6}Li isotope contrast of the $^6LiNbO_3$ layers as a function of multilayer storage time at room temperature (300 K) presented in Figure 6 of the article was calculated as follows

$$K(t = 5\ \text{days}) = \frac{\chi(t = 5\,\text{days}) - \chi_{min}}{\chi(t = 5\,\text{days}) - \chi_{min}} = 100\,\% \qquad (4)$$

$$K(t = 210\ \text{days}) = \frac{\chi(t = 210\,\text{days}) - \chi_{min}}{\chi(t = 5\,\text{days}) - \chi_{min}} \qquad (5)$$

$$K(t = 2005\ \text{days}) = \frac{\chi(t = 2005\,\text{days}) - \chi_{min}}{\chi(t = 5\,\text{days}) - \chi_{min}} \qquad (6)$$

The formulas (5) and (6) were applied for each $^6LiNbO_3$ layers of multilayer with carbon spacer layers except for surface and $^6LiNbO_3$ layer adjacent to the Si wafer substrate. I.e. from each depth profiling we obtained 9 values of Li isotope contrast. The data plotted in Figure 6 of the article and Fig. S11 corresponds to the calculated mean value and standard deviation of ^{6}Li isotope contrast.

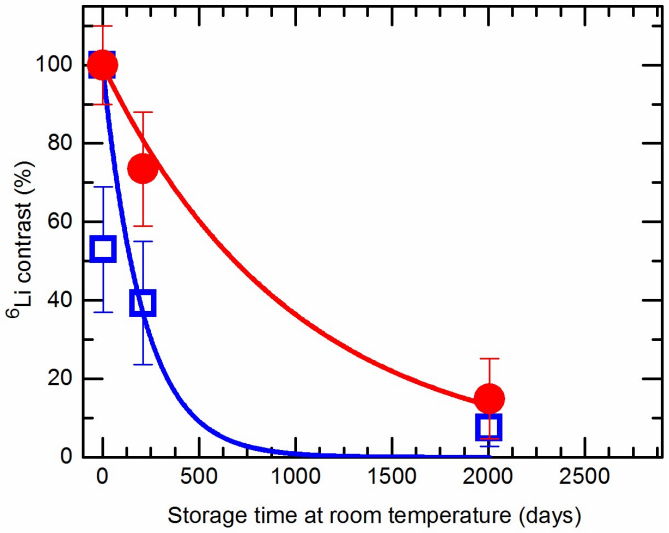

Figure S11: ^{6}Li contrast of the $^6LiNbO_3$ layers as a function of ML storage time at room temperature (300 K) as obtained from SIMS depth profiles performed on the ML with C spacer layers. The lines represent the fit of Eq. (2) to measured data.

The blue open squares in Figure S11 presents Li isotope contrast change calculated with eq. (2) with the assumption that the ML sputter-deposition procedure does not intermix any Li isotopes and the Li isotope intermixing appears solely from a fast Li permeation at room temperature, i.e. for $\chi_{max} = \chi(t = 0 \text{ days}) = 90$ %. However, the fit of eq. (2) to the blue open squares is not of success. This indicates that the ML sputter-deposition process strongly intermixes Li isotopes in the ML with C spacer layers.

5. Neutron reflectometry

The analysis of neutron reflectivity curves (Fig. 7 and Tab.1 of article) enables the determination of the neutron scattering length density (SLD) of the layers. The SLD of a single layer in the multilayer is given by

$$SLD = \frac{N_a \rho}{M} \sum_i b_i \qquad (7)$$

where M is the molecular weight of the compound or element, N_a is Avogadro's number, ρ is the mass density and b_i is the bound coherent scattering length of the i^{th} type atom in the layer. Simplified spoken, the SLD describes the density weighted neutron scattering behavior of that layer.

The SLD is dependent on the mass density, chemical (chemical formula) and isotope composition. So, if the mass density is known, the chemical composition can be roughly determined.

The third raw of Tab. S1 presents the neutron SLD calculated using the mass density existent in the literature for elemental chromium and for different chromium-oxides. Remarkable, the neutron SLD of (3.1 ± 0.1) × 10^{-6} Å^{-2} obtained from the measured NR pattern corresponds well with that of elemental chromium. Oxygen incorporation increase the SLD. Lithium incorporation in chromium-oxide should reduce the SLD of chromium-oxide, but not to the value measured by NR (see Tab. S1). The measured neutron SLD of 3.1 × 10^{-6} Å^{-2} can be explained by chromium oxide only if the mass density is strongly reduced for up to 40%. Roughly spoken, the analysis of neutron reflectivity curves gives evidence of Cr-metal inside the Cr spacer layers.

Table S1: Mass density and neutron SLD for bcc Cr metal and different chromium oxides. The Li isotope fraction in $LiCrO_2$ is considered to be that of the whole superlattice after full Li isotope intermixing which corresponds to $^6Li_{0.54}{}^7Li_{0.46}CrO_2$. The second raw lists mass densities given in the literature for crystalline structures. The mass density of $LiCrO_2$ is taken form Ref. [95]. The third raw lists neutron scattering length densities calculated from mass densities given in the literature (second raw). The last raw lists mass densities which build up the measured neutron SLD of 3.1 × 10^{-6} Å^{-2} of Cr spacer layers.

material	bcc Cr metal	Cr_3O	CrO	Cr_2O_3	CrO_2	CrO_3	$LiCrO_2$
mass density (g/cm^3)	7.14	--	--	5.2	4.9	2.7	4.3
neutron SLD (10^{-6} Å^{-2})	3.01	--	--	5.09	4.79	3.43	4.28
mass density (g/cm^3) for SLD = 3.1 × 10^{-6} Å^{-2}	7.36	5.40	3.80	3.17	2.84	2.45	3.12

Table S2: Parameters used for the simulation of the reflectivity pattern presented in Fig. S12, based on the Parratt32 code. The superlattice consists of ten times [$^6LiNbO_3$ /Cr/$^6LiNbO_3$/Cr/$^{nat}LiNbO_3$/Cr / $^{nat}LiNbO_3$/Cr] eight layer units.

	layer	SLD (10^{-6} Å^{-2})	thickness (nm)	roughness (nm)
air	air	0	--	--
capping	$^{6}LiNbO_3$	4.45	9.0	3.0
multi-layer × 10	Cr	3.1	5.0	1.8
	$^{nat}LiNbO_3$	3.9	4.5	1.8
	Cr	3.1	3.2	1.8
	$^{nat}LiNbO_3$	3.9	4.5	1.8
	Cr	3.1	5.0	1.8
	$^{6}LiNbO_3$	4.45	4.4	1.8
	Cr	3.1	3.2	1.8
	$^{6}LiNbO_3$	4.45	4.5	1.8
Si-wafer	Si	2.07	--	0.5

Table S3: Parameters used for the simulation of the reflectivity pattern presented in Fig. S13, based on the Parratt32 code.

	layer	SLD (10^{-6} Å^{-2})	thickness (nm)	roughness (nm)
air	air	0	--	--
capping	$^{6}LiNbO_3$	4.45	9.0	3.0
multi-layer × 10	Cr	3.1	5.0	0.2
	$^{nat}LiNbO_3$	3.9	4.5	0.2
	Cr	3.1	3.2	0.2
	$^{nat}LiNbO_3$	3.9	4.5	0.2
	Cr	3.1	5.0	0.2
	$^{6}LiNbO_3$	4.45	4.4	0.2
	Cr	3.1	3.2	0.2
	$^{6}LiNbO_3$	4.45	4.5	0.2
Si-wafer	Si	2.07	--	0.5

Table S4: Parameters used for the simulation of the reflectivity pattern presented in Fig. S14, based on the Parratt32 code.

	layer	SLD (10^{-6} Å^{-2})	thickness (nm)	roughness (nm)
air	air	0	--	--
capping	$^{6}LiNbO_3$	4.45	9.0	3.0
multi-layer × 10	Cr	3.1	6.2	1.8
	$^{nat}LiNbO_3$	3.9	4.5	1.8
	Cr	3.1	2.0	1.8
	$^{nat}LiNbO_3$	3.9	4.5	1.8
	Cr	3.1	6.2	1.8
	$^{6}LiNbO_3$	4.45	4.4	1.8
	Cr	3.1	2.0	1.8
	$^{6}LiNbO_3$	4.45	4.5	1.8
Si-wafer	Si	2.07	--	0.5

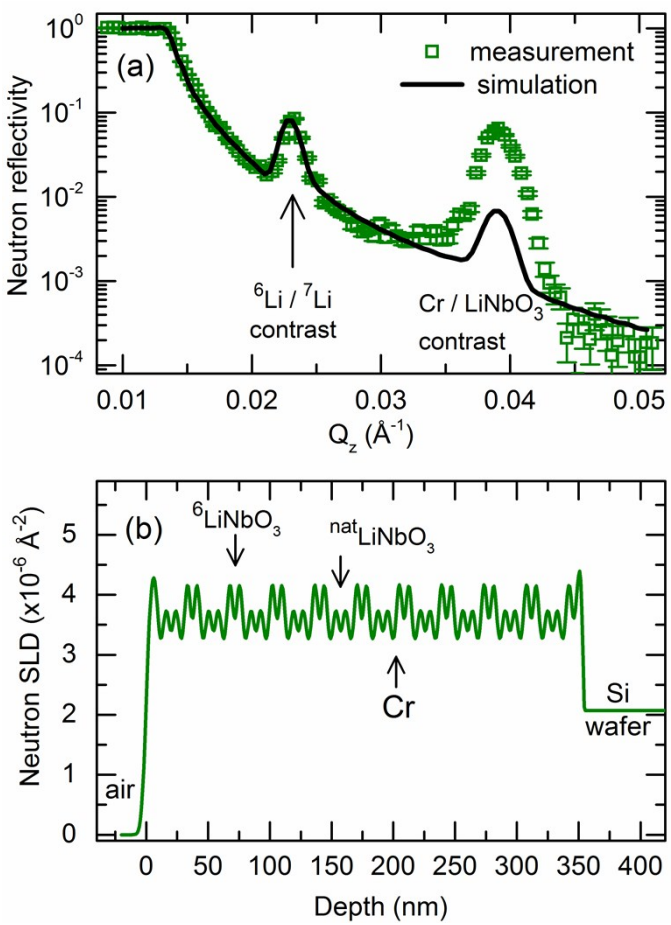

Figure S12: (a) Measured and simulated NR pattern for the superlattice with Cr spacer layers. Simulation performed with a double peaked neutron SLD of the $LiNbO_3$ layers. (b) Neutron scattering length density used for simulation and obtained from the parameters given in Tab.S2.

In the following, it is shown that the double peak structure measured in SIMS (see Fig. S8) is not present in the ML network. To the first, it will be shown that NR is capable of detecting a double peak structure if present. We will test it by assuming double peak structure and calculating its reflectance. Further it will be shown that the double peak structure has no influence on the NR Bragg peak appeared due to the Li isotope ratios.

The double peak structure for NR simulations is designed in accordance to the SIMS depth profile by inserting a 3.2 nm thin Cr layer in the middle of each $LiNbO_3$ layer (except for the capping layer). The total thickness of the Cr layers is maintained constant, i.e., the thickness of the additional Cr layers is subtracted from the former Cr layers (compare Tab.1 of the main article with Tab.S2) (8.2 nm – 3.2 nm = 5 nm). The corresponding neutron SLD is presented in Fig.S12b.
Figure S12a presents the corresponding simulated NR pattern in comparison to the measured NR pattern. The scattering wave vector (Q_z) position of the total reflection edge and of the Bragg peaks is not changed by the double peaked structure, because the total amount of Cr (3.2 nm + 5 nm = 8.2 nm) and $LiNbO_3$ material does

not change and because the periodicity distance (the periodicity lengths in the ML also does not change. Interestingly, on the one hand, the Bragg peak which appears due to the Li isotope contrast is not affected by the double peak structure. On the other hand, the Bragg peak due to chemical contrast is strongly damped and, obviously, does not resemble the measured NR pattern.

Figure S13 shows that the damped Bragg peak due to the double peaked structure cannot be increased (to resemble the measured pattern) by other parameters such as reduced interface roughness (Tab. S3). The Bragg peak is only marginally increased. Figure S14 presents the simulation with a thinner Cr layer inserted inside the $LiNbO_3$ layer (see Tab.S4). The total amount of Cr is again not changed (2 nm + 6.2 nm = 8.2 nm). The Bragg peak increases for a lower amount of Cr present in the middle of the $LiNbO_3$ layers. The simulated Bragg peak resembles the measured one in the case there is no Cr layer in the middle of the $LiNbO_3$ layer (as presented in Figure 5 of the main article).

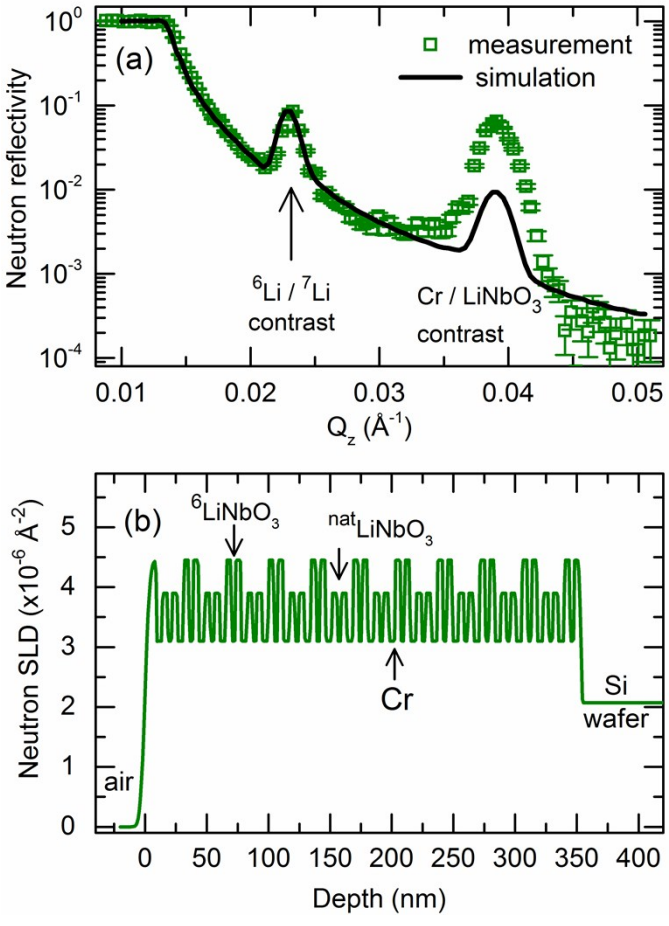

Figure S13: (a) Measured and simulated NR pattern for the superlattice with Cr spacer layers. Simulation performed with a double peaked neutron SLD of the $LiNbO_3$ layers. (b) Neutron scattering length density used for simulation and obtained from the parameters given in Tab.S3.

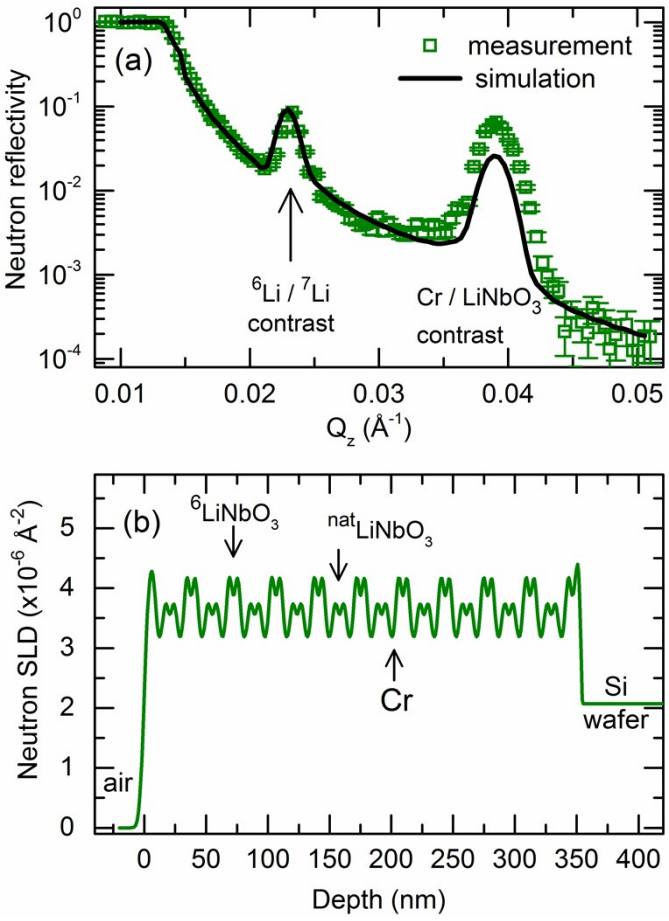

Figure S14: (a) Measured and simulated NR pattern for the superlattice with Cr spacer layers. Simulation performed with a double peaked neutron SLD of the $LiNbO_3$ layers. (b) Neutron scattering length density used for simulation and obtained from the parameters given in Tab.S4.

Figure S15 presents the NR pattern measured from the multilayer with carbon spacer layers after 220 days of ML storage in air and at room temperature. The Bragg peak due to the Li isotope contrast is strongly damped in agreement with the poor Li isotope contrast obtained by SIMS (Figure S10e,f).

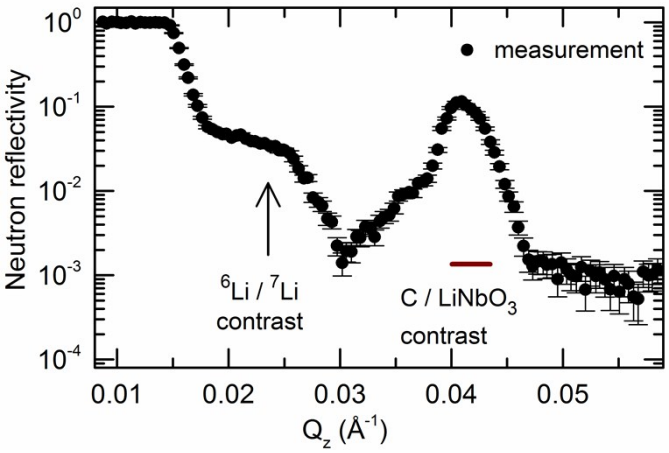

Figure S15: NR pattern measured from the ML with C spacer layers after 220 days of storage in air and at room temperature. The horizontal brown line below the Bragg peak marks the position of the Bragg-peak base line.

Reflectometry is sensitive to interlayer roughness. This is exemplified in Figure S16 for the superlattice with Cr spacer layers. The interface roughness reduces the Bragg peak due to the Cr/$LiNbO_3$ chemical contrast. The Bragg peak due to the Li isotope contrast is less affected.

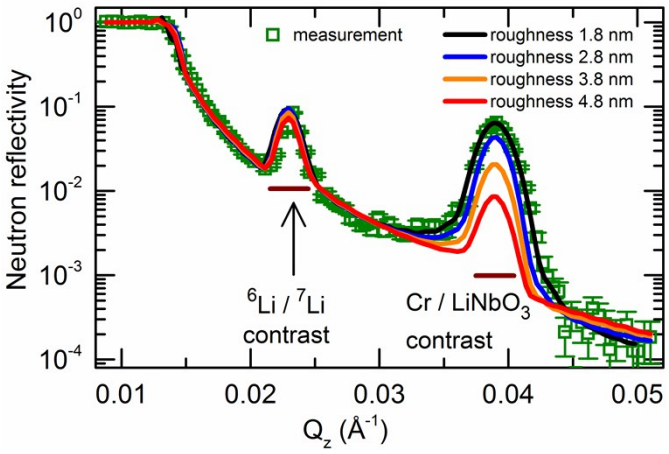

Figure S16: Measured and simulated NR pattern for the superlattice with Cr spacer layers. Simulation was performed for different values of interface roughness. The horizontal brown line below the Bragg peaks marks the position of the Bragg-peak base lines.

Figure S17 presents the behavior of the Bragg peak strength versus the interface roughness. The strength is calculated as the intensity ration of the peak maxima and of the base line. The horizontal brown line below the peaks in Figure S15 and S16 marks the position of the base lines. The Bragg peaks strength of the ML with Si and C spacer layers is also plotted in Figure S17b. The measured NR pattern can be explained only if the layers were fairly smooth. Let mention that the interface roughness investigated by reflectometry correspond to a average roughness value. Investigation with local resolution by transmission electron microscopy would be of great desire.

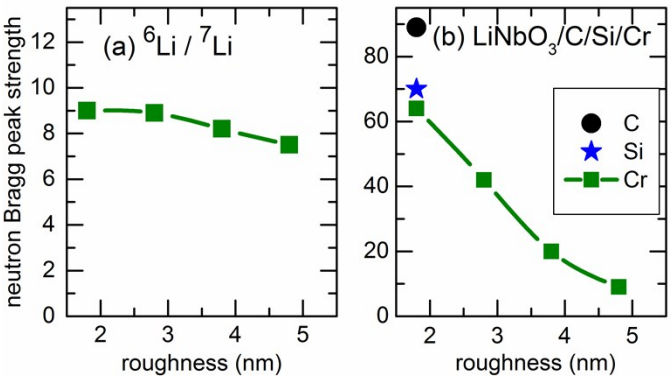

Figure S17: Interlayer roughness dependence of the strength of neutron Bragg peaks appeared due to (a) Li isotope contrast and (b) due to chemical contrast. The strength was calculated by the fraction between the intensity of the peak maxima and base line (marked with horizontal brown lines in Figure S15 and S16). The values at a roughness of 1.8 nm correspond to measured patterns, the other ones to simulated patterns. The Bragg peaks strength of the ML with Cr, Si and C spacer layers are plotted with dots, stars and filled squares, respectively.

6. Grazing incidence X-ray diffraction

Grazing-incidence X-ray diffraction (GI-XRD) found the multilayer with Si spacer layers to be X-ray amorphous. This is not the case for the superlattice with Cr spacer layers. Figure S18 presents the GI-XRD measurements [96] performed on superlattice with Cr spacer layers in comparison to that obtained from the Cr sputter target used to deposit the Cr spacer layers. Body centred cubic chromium is found by GI-XRD in the superlattice without any evidence of crystalline chromium oxides or $LiCrO_2$ [87,88,97-107]. GI-XRD measurement reveals that the Cr spacer layers are polycrystalline with grains of bcc Cr crystal structure. So, Cr-metal exists in the Cr spacer layers inside the bcc grains.

The GI-XRD Bragg peaks obtained from the superlattice are small and broad compared to that obtained from the bulky Cr sputter target (Figure S18).

A Williamson-Hall [108] analysis (Figure S18b) of the GI-XRD data reveals the size of the bcc Cr grain to amount to (9 ± 1) nm which is only slightly larger than the thickness of the Cr spacer layer obtained by NR. The minute larger value fits well with the fact that GI-XRD monitor the average grain size oblique to the surface normal [96]. Very probably the Cr grains are of columnar shape parallel to the surface normal. Often, ion beam sputtering deposition of metals results in polycrystalline films with columnar grains oriented perpendicular to the surface [99].

Using the bulk modulus of chromium, a micro-stress in the Cr grains of 12 GPa is obtained from the Williamson-Hall analysis (Figure S18b). This is a high value. For example, the stress values which are measured during lithiation of silicon thin films are in the range of 1 to 2 GPa [109-117]. It is supposed that such stresses are responsible for the pulverization of Si electrodes during Li-ion battery operation. As measured, the produced superlattice withstands one order of magnitude higher stresses. For pure reason of strength comparison, let mention that the stress of 12 GPa is achieved by bending with a (high) curvature radius of 0.025 m a 9 nm thin Cr coat on 100 µm thin Si wafer.

The GI-XRD measurement of annealed sample at 100 °C for 11 hours (see Figure S18) is of special interest. The thermal expansion of the layers differs one from the other and also differs from that of the substrate. Thermo-elastic stress can appear in multilayer during heating. If thermal energy is available, stress relaxation processes can also take place by annealing. When heating up the sample, the interatomic distances changes due to reversible thermo-elastic expansion and due to

irreversible relaxation [118] which can change the GI-XRD pattern. This is not the case for the described Li permeation experiments. The measured GI-XRD pattern does not change after annealing the superlattice. Also the results obtained from the Williamson Hall analysis, i.e. grain size and micro-stress, is not changed (within the experimental errors) by the annealing procedure. This means that the annealing at 100 °C does not change any reversible and any irreversible strains. Lithium permeation takes place at 100 °C in a frozen and strained multilayer without any change of structure, chemistry and micro-stress.

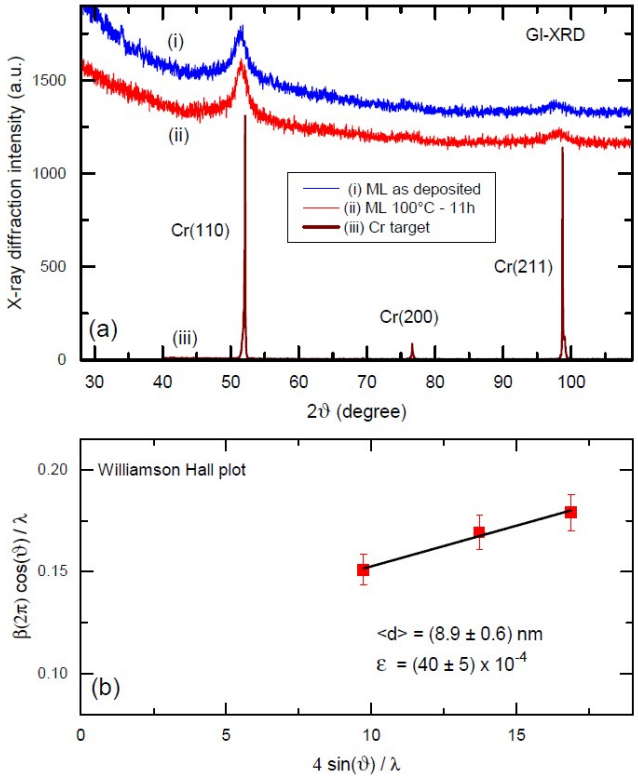

Figure S18: (a) Grazing incidence X-ray diffraction patterns obtained from the superlattice with Cr spacer layers in the as-deposited state and after annealing at 100°C for 11 hours. The GI-XRD pattern of the Cr target is also presented. The curves are shifted in intensity for better visualisation. **(b)** Williamson-Hall plot obtained from the GI-XRD pattern measured on the superlattice with Cr spacer layers. Considering an elastically regime (where Hook's law with $\sigma = E \times \varepsilon$ is guilty) the measured strain $\varepsilon = 0.04 \pm 0.0005$ results in a stress of $\sigma = (11.5 \pm 1.5)$ GPa inside the Cr spacer layers (considering the elasticity modulus of chromium E = 289 GPa and $\sigma = E \times \varepsilon$).

The measured stress existing in the superlattice with Cr spacer layers may attend from interfaces, i.e. from the bond of Cr layers to lithium niobate layers and, probably, also from defects and the pressure of the grain boundary exercised on the Cr-metal columnar grains. Nevertheless, the Cr spacer layers are in proximity with an oxide (lithium niobate). So, it can be expected that Cr-O bonds should be present on the Cr/$LiNbO_3$ interface and even in the grain boundary regions. The latter would explain the higher Li permeation through Cr spacer layers in respect to that through the Si spacer layers. Oxides possess high Li solubility S (uptake) in comparison to elemental silicon and chromium. Consequently, Li permeability P can be enhanced through oxidized regions considering P=S×D, with S and D Li solubility and diffusivity, respectively. Fast Li permeation through the Cr spacer layers can take place via the, assumable, oxidized grain boundaries of the polycrystalline Cr spacer layers due to a higher Li solubility in oxidized regions.

7. FTIR and Raman scattering

Raman spectroscopy provides the ability to analyze all carbon structures (graphite, diamond, graphene, nanotube, fullerene) [142-146]. Figure S19 presents the Raman spectra of the multilayer with C spacer layers. It strongly resembles the typical Raman spectra of amorphous carbon with low content sp^3 structure. Amorphous carbon films are assumed to possess intermediate structures between graphite (fully sp^2) and diamond (fully sp^3). In literature, ion beam sputter deposited carbon films were found to possess a more graphitic like structure, i.e. low sp^3 amorphous carbon.

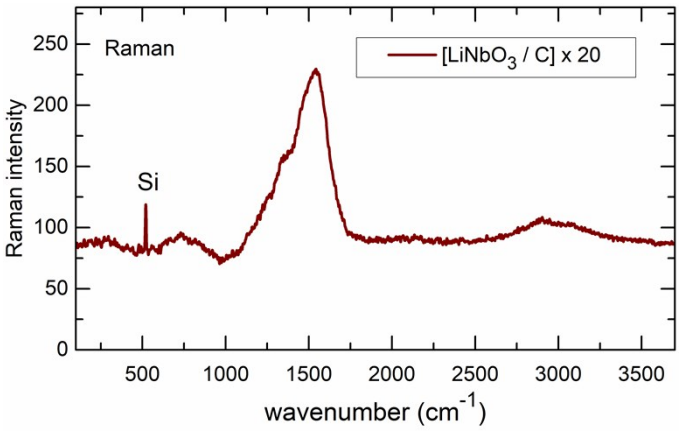

Figure S19: Raman spectra measured from the as deposited multilayer with C spacer layers.

Figure S20 presents the FTIR and Raman scattering results measured from superlattice with Cr spacer layers after the Li permeation experiments at 100 °C were performed. The FTIR and Raman scattering measurements on a standard (reference) Cr_2O_3 sample are also shown for reason of comparison.

The FTIR spectra from the superlattice shows strong interference peaks (fringes) due to constructive and destructive interference of the infrared beams reflected on the air-superlattice and superlattice-substrate interfaces. FTIR signals from chromium oxide [100,104-107] cannot be discerned. The Raman spectra from the Cr_2O_3 reference sample shows a sharp peak at 560 cm^{-1}, which is absent in the Raman measurement performed on the superlattice. The reference material Cr_2O_3 was polycrystalline. Chromium oxide could not be evidenced

in FTIR and Raman scattering measurements [102,103,119-121]. The reason could be an amorphous nature of the chromium oxide in the superlattice. Materials in amorphous network shows often strongly damped FTIR and Raman signals in comparison to that recorded from materials with crystalline structure [122].

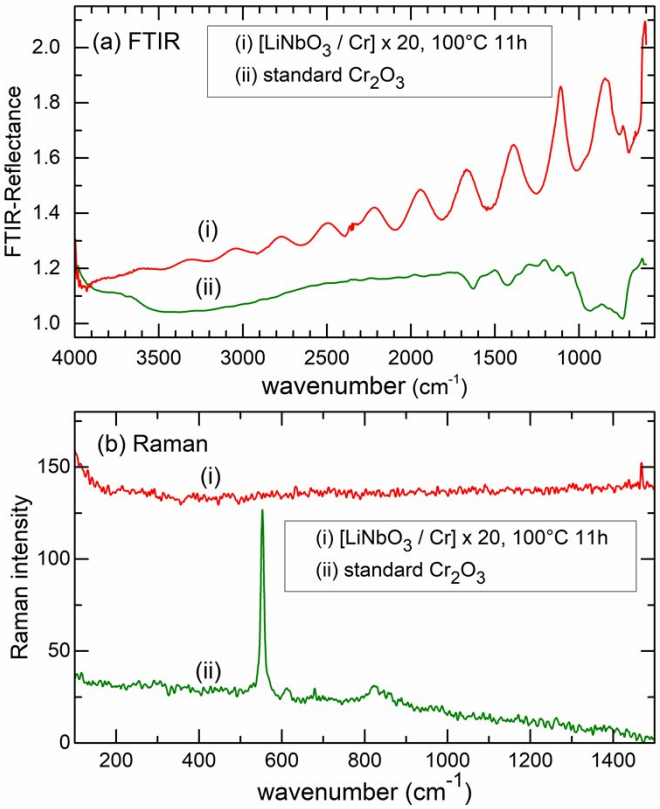

Figure S20: (a) FTIR reflectance spectra taken from the superlattice with Cr spacer layers after annealing at 100 °C for 11 hours and that of a standard Cr_2O_3 sample. The FTIR reflectance of Cr_2O_3 sample is shifted to higher values by an amount of 1.0 for better data representation. **(b)** Raman spectra of the multilayer with Cr spacer layers after annealing at 100 °C for 11 hours and that of a standard Cr_2O_3 sample. The Raman data of the multilayer sample is shifted to higher values by an amount of 110 for better data representation.

8. *In-situ* X-ray absorption spectroscopy

Short range order suffices to X-ray absorption spectroscopy (XAS). Hence, XAS can be used to investigate the existence of chromium-oxide bonds even in an amorphous network [123]. X-ray absorption spectroscopy has become a routine tool that can reveal highly localized element specific information on the electronic structure of atoms in complex environments. XAS focuses on the electronic transition where a core electron is excited to the manifold of unoccupied states. Oscillations χ(k), measured in XAFS as presented in Fig. S18 (see the right panels of the figure), are due to the interference of photoelectron wave coming from the absorber atom and backscattered waves from the neighbouring atoms where various scattering paths contribute. The shape of χ(k) is determined by the local environment around a specific element. χ(k) contains information on the neighbouring type of atoms, the inter-atomic distances and the coordination number. Further advantages of XAFS are: sensitivity to dilute elements; requires relatively short times to collect experimental spectra (from milliseconds to tens of minutes) using synchrotron radiation; and, requires small sample volumes for data analysis [123].

However, due the limited minute material content within the investigated superlattice which possesses ultrathin layers and strong screening effect, the collected XAFS data suffers from poor signal to noise ratio. XAFS measurements were performed also *in situ* during heating the superlattice in air at 100° C. Enhanced noise usually at higher k (higher energy) values, where chromium-oxide is detected [88,124-126], is also a factor. The data of Figure S21 has been averaged for every 3 hours during the annealing process at 100 °C. The spectral data were split into 5 groups: pre-annealed, 0-3 hrs annealed, 4-6 hrs annealed, 7-9 hrs annealed, and 10-12 hrs annealed.

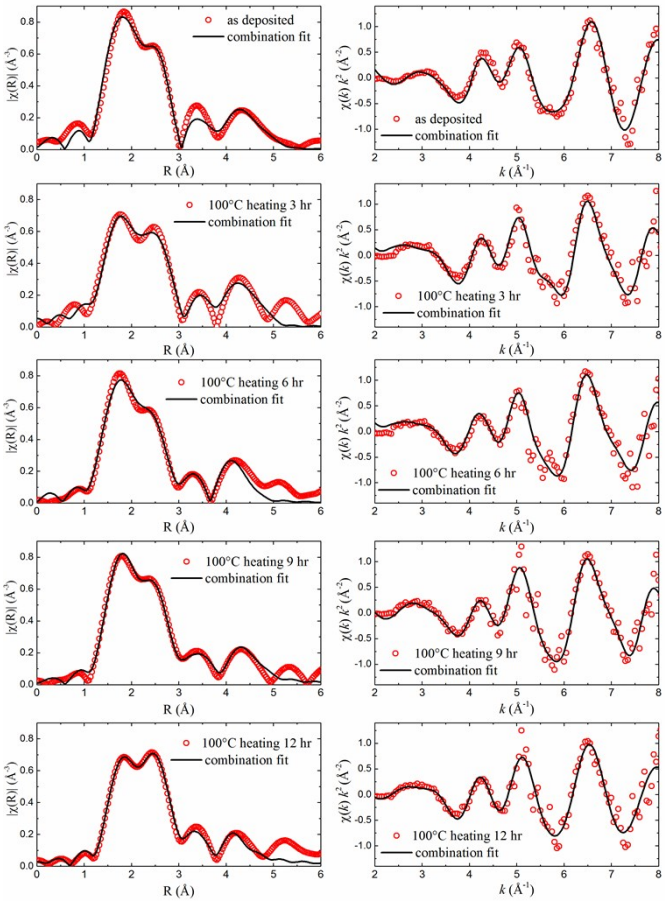

Figure S21: XAFS measurement at Cr K edge signal recorded *in situ* during heating the superlattice with Cr spacer layers in air at 100 °C. Right panels: XAFS χ(k) spectra. Left panels: the Fourier transform of the XAFS spectra. The XAFS measurements are marked with symbols, whereas the fit to the data using a combination of bcc Cr and Cr_2O_3 structures is given with solid lines.

A Fourier transform of the measured XAFS data (left panels of Figure S21) shows peaks representative of the different scattering paths of the photoelectron**.** Hence, a radial distribution function is obtained. From that, the bonding lengths of Cr to the next atoms in local environment are obtained. In order to extract information about the local environment of the absorber, however, the backscattering amplitude and phase shift functions are needed [127]. The latter is a sum of contributions from the absorber, and from the scattering atom. These functions cause peaks for a particular shell in the Fourier transform of χ(k) (left panels of Fig. S21) to be shifted 0.2 - 0.5 Å below the actual interatomic distances. This is also observed for the XAFS data collected from Cr-metal and Cr_2O_3 reference materials (Fig. S22). A polycrystalline Cr_2O_3 that obtained from Sigma Aldrich was used as a reference standard and model for fitting.

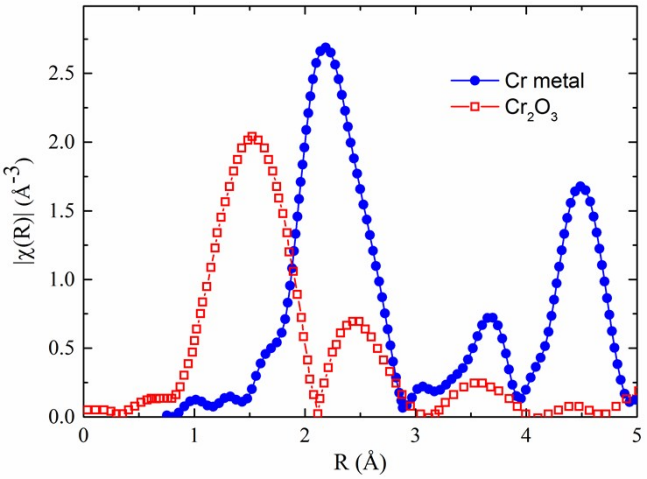

Figure S22: XAFS measurement at Cr K edge signal recorded from Cr-metal and Cr_2O_3 reference samples.

Figure S22 shows that the measured EXAFS data from the superlattice (Fig. S21) is a mixture of signals from Cr -metal and Cr-oxide bonding environment.

In order to obtain percentage of Cr -metal and Cr-oxide bonding environment, the EXAFS spectra were fitted.

The amplitude and phase shift functions can be obtained experimentally from EXAFS spectra of model compounds. However, obtaining an appropriate model compound similar to the superlattice under investigation and extracting the amplitude and phase functions may be difficult. They can be also calculated with a degree of accuracy sufficient for most applications.

Two different models were used in the XAFS fitting**.** The first one is by considering only Cr-metal [128-132] in the model, and the second by considering Cr_2O_3 in the model**.** It was found that the second model (termed combinational model) yields a better fit in the high k-values range, meaning that the system contains, beside Cr-metal, also some Cr-oxide**.** For the fits, the following function were used

$$\chi(k) = \sum_j \frac{S_0^2 N_j}{k R_j^2} \left| F_j(k,\pi) \right| \sin\left[2kR_j + \varphi_j(k) \right] e^{-2\sigma_j^2 k^2} e^{-2R_j/\lambda(k)} \quad (8)$$

where k is the photoelectron wavenumber. Note that k is really the 'photoelectron momentum index' and differs from the physical momentum. The normalised value of χ(k) is dimensionless, because the (standard) expression above has F in units of 1/ k (i.e. length). Other definitions for F being dimensionless (as a form factor or scattering amplitude) have $(kR)^2$ in the denominator to maintain consistency of units.

The sum in the EXAFS equation is most simply over shells of atoms of a particular type j and similar distances from the origin of the initial photoelectron. Then N_j is the coordination number, R_j the interatomic distance, and σ_j^2 represents the mean-square disorder in the distance for the jth shell. Fj is the photoelectron (back-) scattering amplitude and φ(k) is the corresponding (back-) scattering phase for the jth atomic shell. S_0^2 is an amplitude reduction factor accounting for relaxation of the absorbing atom due to the presence of the empty core level and multi-electron excitations. λ(k) is the photo-electron inelastic mean free path, which has a strong dependence upon k, and has values in the range of 1 to 100 Å over the XAFS regime. The crude approximation of $\varphi(k) = 2\pi a_0$ (a_0 is the Bohr radius) works for many systems and causes peaks for a particular shell in the Fourier transform of χ(k) to be shifted ~ 0.2 - 0.5 Å below the actual interatomic distance. Both Fj(k) and φ(k) depend upon the atomic number Z of the scattering atom, and have non-linear dependence on k.

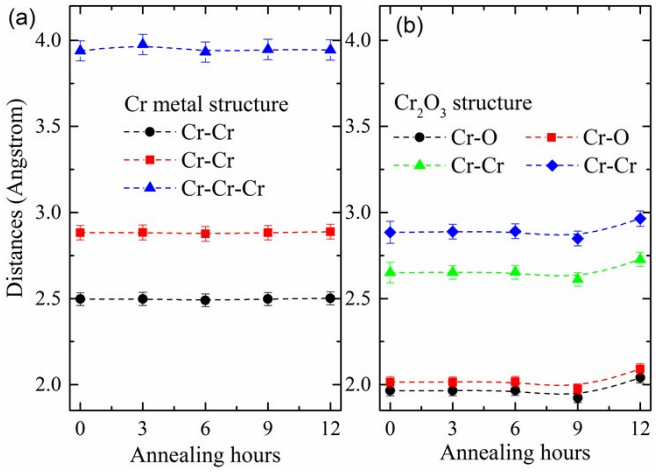

Figure S23: Path (R): interatomic distances for Cr metal **(a)** and chromia **(b)** extracted from the fitted data in dependence of the annealing time at 100 °C.

The fits to the data using a combination of bcc Cr and Cr_2O_3 structures is given with solid lines in Fig. S21. Since the Fourier transform was performed without the phase-shift corrections, this would result in a shift in peak position to lower distance (~ 0.2 - 0.5 Å, depending upon the atomic number) with respect to the actual inter-

atomic distance. Therefore, the distance shown on the graph should be added with the value of 0.2 - 0.5 Å to obtain the actual inter-atomic distance. The data clearly show that there are both Cr-metal and oxidized Cr species in superlattice, which is also tabulated in Tab. S5 and presented in Fig. S22. The percentage of Cr-metal and Cr_2O_3 is listed in Tab.S5 (as square of S_0) varying between 75-85% for Cr-metal and the rest for Cr_2O_3.

It is obvious that the proximity of the Cr layers to oxide layers ($LiNbO_3$) produces chromium oxide bonds at least at the interfaces. The analysis shows that 15-25 percent of Cr bonds are in oxidized environment. If these bonds are situated on the interface to $LiNbO_3$, then the thickness of the Cr oxide interface layers should be less than 1 nm. These interface layers were taken into account during the NR analysis by considering in the fits a roughness value of 1.8 nm in between the Cr and $LiNbO_3$ layers (see Tab.1 of article). However, the XAFS study cannot discern if chromium oxide stems from the Cr layers, interfaces or from Cr atoms within the $LiNbO_3$ layers.

Concluding, the analysis of the XAFS data reveals (i) existence of Cr oxide bonds, (ii) most of Cr bonds (some 80 percent) are in the Cr metallic structure, and (iii) annealing in air at 100°C does not change the Cr bonding environment.

Table S5: the scattering path, degeneracy of path (*N*), the passive electron reduction factor (S_0^2), the path length (*R*), and the mean squared displacement (σ^2) extracted from the fitted data for superlattice with Cr spacer layer in combination fit of Cr metal and Cr_2O_3 structures.

Sample	Cr metal structure						Cr_2O_3 structure					
	scattering path	*N*	S_0^2	*R*	σ^2	R-factor	scattering path	*N*	S_0^2	*R*	σ^2	R-factor
0h	Cr-Cr	8	0.752	2.497	0.0149	0.026	Cr-O	3	0.248	1.965	0.0030	0.026
		6	0.752	2.883	0.0165			3	0.248	2.015	0.0030	
	Cr-Cr-Cr	24	0.752	3.939	0.0210		Cr-Cr	1	0.248	2.651	0.0030	
								3	0.248	2.885	0.0030	
3 hr	Cr-Cr	8	0.814	2.498	0.0210	0.031	Cr-O	3	0.186	1.965	0.0030	0.031
		6	0.814	2.884	0.0176			3	0.186	2.015	0.0030	
	Cr-Cr-Cr	24	0.814	3.976	0.0210		Cr-Cr	1	0.186	2.652	0.0030	
								3	0.186	2.889	0.0030	
6 hr	Cr-Cr	8	0.778	2.490	0.0184	0.023	Cr-O	3	0.222	1.967	0.0030	0.023
		6	0.778	2.876	0.0242			3	0.222	2.018	0.0030	
	Cr-Cr-Cr	24	0.778	3.932	0.0107		Cr-Cr	1	0.222	2.653	0.0030	
								3	0.222	2.891	0.0030	
9 hr	Cr-Cr	8	0.848	2.497	0.0185	0.008	Cr-O	3	0.152	1.924	0.0030	0.008
		6	0.848	2.883	0.0184			3	0.152	1.975	0.0030	
	Cr-Cr-Cr	24	0.848	3.947	0.0176		Cr-Cr	1	0.152	2.611	0.0030	
								3	0.152	2.849	0.0030	
12 hr	Cr-Cr	8	0.836	2.502	0.0195	0.007	Cr-O	3	0.164	2.040	0.0030	0.007
		6	0.836	2.889	0.0190			3	0.164	2.091	0.0030	
	Cr-Cr-Cr	24	0.836	3.944	0.0170		Cr-Cr	1	0.164	2.727	0.0030	
								3	0.164	2.965	0.0030	

9. Magnetic behavior

As described in the article a weak ferromagnetic signal at room temperature was measured for the multilayers with Cr and Si spacer layers but not for that with carbon spacer layers. Hence, a ferromagnetic spin alignment caused by Cr and Si elements in the multilayers with Cr and Si spacer layers cannot be ruled out. Some traces of Cr and Si can exist inside $LiNbO_3$ which can be on the origin of ferromagnetic order at room temperature (300 K) measured in this work on multilayers with Cr and Si spacer layers, respectively.

If it is of interest, e.g. for the field of spintronics, then further magnetic investigations can be performed on the class of multilayers presented in this work. Such forthcoming experiments could investigate the influence of (i) layer chemistry and layer thicknesses, (ii) additional mechanical stress imposed on the multilayers by using sample bending devices, (iii) annealing temperature and annealing time interval of $LiNbO_3$

multilayers with Si, Cr (and other metals such as Rh and Pd) spacer layers. For the 4d metals Rh and Pd let mention that first principle density functional theory calculations predict ferromagnetic order at the equilibrium lattice constant if Rh is in bcc and Pd in hcp crystal structure [72-76]. Stress, impurity and confinement, as it is present in multilayers, may change the crystal structure of spacer layers to induce ferromagnetic order in metals with non-ferromagnetic order in native crystal structure. For reason of comparison, magnetic investigations should then be performed on $LiNbO_3$ superlattices with spacer layers of ferromagnetic material, e.g. iron, cobalt and nickel. The Li permeation and stress experiments should be extended to investigate the influence of spacer layer thickness and temperature. Furthermore, the influence of frozen-in defects annihilation on (i) Li permeation and (ii) magnetic order merits also investigations. The $LiNbO_3$ superlattices with metallic spacer layers would/should possess amorphous $LiNbO_3$ layers and nano-crystalline spacer layers and, hence, be full of frozen-in defects. The atomic diffusion in as-deposited amorphous and nano-crystalline films was measured to be time dependent due to annihilation of frozen-in defects [7,9,133-136]. This is traced back to the existence of frozen-in defects which leads to fast diffusion. Annealing annihilates these defects by structural relaxation which slows down diffusion. Diffusivities decays over more than 3 orders of magnitude were measured for Si self-diffusion in amorphous silicon [137]. Last but not least, electrical measurements to investigate space charge layers are also desirable. One may note that, due to the ultrathin fashion of the layers, the space charge layer can extend throughout the entire ultrathin layers [140,141]. An electric field over the spacer layer can appear also due to the piezoelectric property of the $LiNbO_3$ layers. The large stress of 12 GPa measured by x-ray scattering (GIXRD) in the Cr spacer layers may be a evidence that the piezoelectric material of the $LiNbO_3$ layers are under strain. The strain can induce a piezoelectric electric field over the (e.g. Cr) spacer layer [138,139] which can affect the electronic structure of the spacer layer. The strain on the $LiNbO_3$ layers which induce the piezoelectric field can be changed by the thickness of the individual layers and the annealing temperature due to, e.g. different thermal expansion coefficients of the materials in the superlattice.

10. Conclusion of superlattice characterization

A full characterization of the as-deposited and annealed superlattice were performed with a plurality of non-destructive measurement techniques including neutron reflectometry (NR), grazing-incidence X-ray scattering (GI-XRD), infra-red spectroscopy (FTIR), Raman scattering and extended X-ray absorption fine structure spectroscopy (EXAFS). Raman scattering found the carbon spacer layers to be amorphous and predominant of graphitic (sp^2) bonding configuration. GI-XRD reveals that the Si spacer layers are amorphous whereas the Cr spacer layers are polycrystalline with elemental bcc chromium. There is no evidence of crystalline Cr-oxide. Chromium oxide was also not detected by FTIR and Raman scattering. Also the neutron scattering length density obtained in NR could be explained only with elemental bcc chromium. EXAFS was performed *in-situ* during Li permeation took place by heating the superlattice at 100°C in air. The EXAFS experiments revealed the Cr bonding environment to be of 80 percent as Cr metal and 20 percent as chromium oxide. There is lack of further oxidation during superlattice heating at 100 °C in air. However, the EXAFS study cannot discern if the measured chromium oxide exists in the Cr layers or stems from Cr atoms within the $LiNbO_3$ layers. All in all, the experiments evidenced that the ultrathin Cr layers are not (fully) oxidized. The measurements further show that the crystallographic network (polycrystalline for Cr layers and amorphous for Si, C and $LiNbO_3$ layers) and the chemistry of the multilayers does not change at all by the performed Li permeation (i.e. annealing) experiments. GI-XRD experiments measured a high stress of 12 GPa acting on bcc Cr grains in the superlattice which does not change by the performed Li permeation experiments. Li permeation was measured (see article) in an, otherwise, conserved multilayer network. Some traces of Cr and Si can exist inside $LiNbO_3$ which can be on the origin of ferromagnetic order at room temperature (300 K) measured in this work on multilayers with Cr and Si spacer layers, respectively.

11. References

[1] Concerning the terminology of superlattice, it is questionable if a multilayer with periodically alternating amorphous individual layers can be called a superlattice. On one hand, if the individual layers are amorphous the multilayer lacks of a crystallographic lattice. On the other hand, the chemically periodicity of the alternating amorphous layers produces very well a chemical periodicity (lattice) perpendicular to the interfaces due to the chemical contrast, which leads to Bragg peaks in small angle scattering (X-ray reflectometry and neutron reflectometry). As it is shown in this work the multilayers of alternating Cr and $LiNbO_3$ possess crystalline (polycrystalline) Cr layers whereas all layers of the multilayers with alternating Si, C and $LiNbO_3$ material are amorphous. Therefore, throughout this work the terminology of superlattice will be used only for multilayers of alternating Cr and $LiNbO_3$ layers and not for the multilayers of alternating Si (C) and $LiNbO_3$ layers. The aforementioned discussion about the usage of the terminology of superlattices to all multilayers with periodically alternating individual layers can be extended also to isotope multilayers. In isotope multilayers the alternating layers possess the same chemistry but different isotopes. Isotope multilayers were produced with oriented crystalline [2-4], polycrystalline [5,6] and amorphous individual layers [7-10]. Due to lack of chemical contrast all isotope multilayers should not produce Bragg peaks in low angle X-ray scattering. This is not the case if the isotopes possess different neutron scattering lengths. For such isotope

multilayers low angle neutron scattering develop Bragg peaks even for a chemically homogeneous amorphous film (with isotope modulation) [3-10]. The multilayers and superlattices described in this work combine both, i.e. a chemical and an isotope modulation. This develops in low angle neutron scattering Bragg peaks appearing solely from the chemical contrast and other Bragg peaks appearing solely due to the isotope contrast.

[2] R. Kube, H. Bracht, E. Hüger, H. Schmidt, J. L. Hansen, A. N. Larsen, J. W. Ager, E. E. Haller, T. Geue, J. Stahn, Phys. Rev. B 88 (2013) 085206.
[3] E. Hüger, R. Kube, H. Bracht, J. Stahn, T. Geue, H. Schmidt, phys. stat. sol. B 11 (2012) 2108.
[4] E. Hüger, U. Tietze, D. Lott, H. Bracht, E. E. Haller, D. Bougeard, and H. Schmidt, Appl. Phys. Lett. 93 (2008) 162104.
[5] H. Schmidt, S. Chakravarty, M. Jiang, E. Hüger, P. K. Parida, T. Geue, J. Stahn, U. Tietze, and D. Lott, J. Mater. Sci. 47 (2012) 4087.
[6] S. Chakravarty, E. Hüger, H. Schmidt, J. Stahn, M. Horisberger, N. P. Lalla, Scripta Mater. 61 (2009) 1117.
[7] H. Schmidt, M. Gupta, T. Gutberlet, J. Stahn, and M. Bruns, Acta Materialia 56 (2008) 464.
[8] E. Hüger, H. Schmidt, T. Geue, J. Stahn, U. Tietze, D. Lott, A. Markwitz, U. Geckle, M. Bruns, J. Appl. Phys. 109 (2011) 093522.
[9] E. Hüger, H. Schmidt, J. Stahn, B. Braunschweig, U. Geckle, and M. Bruns, Phys. Rev. B. 80 (2009) 220101.
[10] H. Schmidt, M. Gupta, and M. Bruns, Phys. Rev. Lett. 96 (2006) 055901.
[11] D. Chen, C. Chen, Z.M. Baiyee, Z. Shao, and F. Ciucci, Chem. Rev. 115 (2015) 9869.
[12] K. Zhu, ACS Energy Lett. 1 (2016) 64.
[13] Y. Yamada, T. Yamada, A. Shimazaki, A. Wakamiya, and Y. Kanemitsu, J. Phys. Chem. Lett. 7 (2016) 1972.
[14] I. Grinberg, D. V. West, M. Torresw, G. Gou, D. M. Stein, L. Wu, G. Chen, E. M. Gallo, A. R. Akbashev, P. K. Davies, J. E. Spanier, and A. M. Rappe, Nature 503 (2013) 509.
[15] D. Raiser, S. Mildner, B. Ifland, M. Sotoudeh, P. Blöchl, S. Techert, and Ch. Joss, Adv. Energy Mater. (2017) 1602174, DOI: 10.1002/aenm.201602174.
[16] M. Sessolo, and H. J. Bolink, Science 350 (2015) 917.
[17] L. Dou, A. B. Wong, Y. Yu, M. Lai, N. Kornienko, S. W. Eaton, A. Fu, C. G. Bischak, J. Ma, T. Ding, N. S. Ginsberg, L.-W. Wang, A. P. Alivisatos, and P. Yang, Science 349 (2015) 1518.
[18] H. Zhou, Q. Chen, G. Li, S. Luo, T.-b. Song, H.-S. Duan, Z. Hong, J. You, Y. Liu, Y. Yang, Science 345 (2014) 542.
[19] J.R. Scheffe, and A. Steinfeld, Materials Today 17 (2014) 341.
[20] A.H. McDaniel, A. Ambrosini, E.N. Coker, J.E. Miller, W.C. Chueh, R. O'Hayre, and J. Tong, Energy Procedia 49 (2014) 2009.
[21] S. Dunn, Thin Solid Films 601 (2016) 59.
[22] N. Galinsky, M. Sendi, L. Bowers, and F. Li, Applied Energy 174 (2016) 80.
[23] M. McMillen, A.M. Douglas, T.M. Correia, P.M. Weaver, M.G. Cain, Appl. Phys. Lett. 101 (2012) 242909.
[24] A.S. Mischenko, Q. Zhang, J.F. Scott, R.W. Whatmore, N. D. Mathur, Science 311 (2006) 1270.
[25] S. Hirose, T. Usui, S. Crossley, B. Nair, A. Ando, X. Moya, N.D. Mathur, APL Mater. 4 (2016) 064105.
[26] G.G. Guzman-Verri, P.B. Littlewood, APL Mater. 4 (2016) 064106.
[27] K. K. Wong (Ed.), Properties of Lithium Niobate, (INSPEC Institution of Electrical Engineers, London, 2002).
[28] M. C. Gupta, and J. Ballato (Eds), The Handbook of Photonics, (CRC Press Taylor & Francis Group, Boca Raton, 2007).
[29] T. Volk, and M. Wöhleke, Lithium Niobate, (Springer, Berlin, 2010).
[30] Y. Kuz'minov, Lithium Niobate Crystals, (Cambridge International Science Publishing, 1999).
[31] Q. Peng, and R. E. Cohen, Phys. Rev. B 83 (2011) 220103.
[32] Issue 4, December 2015 of Appl. Phys. Rev. 2 (2016) Contributions to the Special Topic: Lithium Niobate: Properties and Applications: Review of Emerging Trends.
[33] V. Pralong, M. A. Reddy, V. Caignaert, S. Malo, O. I. Lebedev, U. V. Varadaraju, B. Raveau, Chemistry of Materials 23 (2011) 1915.
[34] M. V. Reddy, G. V. Subba Rao, B. V. R. Chowdari, Chemical Reviews 113 (2013) 5364.
[35] M. V. Reddy, U. V. Varadaraju, J. Phys. Chem. C 115 (2011) 25121.
[36] Q. Fan, L. Lei, G. Yin, Y. Sun, Chem. Commun. 50 (2014) 2370.
[37] Q. Fan, L. Lei, Y. Sun, Nanoscale 6 (2014) 7188.
[38] Z. Jiang, X. Lu, Z. Fang, Y.-S. Hu, J. Zhou, W. Chen, L. Chen, Electrochemistry Commun. 13 (2011) 1127.
[39] H. Xu, J. Shu, X. Hu, Y. Sun, W. Luo, Y. Huang, J. Mater. Chem. A 1 (2013) 15053.
[40] V. Augustyn, J. Come, M. A. Lowe, J. W. Kim, P.-L. Taberna, S. H. Tolbert, H. D. Abruna, P. Simon, B. Dunn, Nature Materials 12 (2013) 518.
[41] V. Augustyn, P. Simon, B. Dunn, Energy Environ. Sci. 7 (2014) 1597.
[42] P. Simon, Y. Gogotski, B. Dunn, Science 343 (2014) 1210.
[43] J. Li, et al., Rare Met. DOI 10.1007/s12598-014-0423-z
[44] Glass, A. M.; Nassau, K.; Negran, T. J.; Ionic conductivity of quenched alkali niobate and tantalate glasses, J. Appl. Phys. 49 (1978) 4808.
[45] Goldner, R. B.; Haas, T. E.; Seward, G.; Wong, K. K.; Norton, P.; Foley, G.; Berera, G.; Wei, G.; Schulz, S.; Chapman, R.; Thin film solid state ionic materials for electrochromic smart window glass, Solid State Ionics 28-30 (1988) 1715.
[46] R. B. Goldner et al., US Patent No. 4,832,463 (1989); European Patent EP03863541 (1990).
[47] R. B. Goldner et al., US Patent No. 6,982,132 B1 (2006).
[48] R. B. Goldner et al., US Patent No. 5,051,274 (1991).
[49] A. M. Glass et al., US Patent No. 4,130,694 A (1989); European Patent EP0000785 B1 (1990).
[50] K. Takada, et al., *Solid State Ionics* 225 (2012) 594.
[51] Ph. Knauth, Solid State Ionics 180 (2009) 911.
[52] Oudenhoven, J. F. M.; Baggetto, L.; Notten, P.; All-solid-state lithium-ion microbatteries, a review of various three dimensional concepts, *Adv. Energy Mater*. 1 (2011) 10.
[53] E. E. Horopanitis, G. Perentzis, P. G. Karagiannidis, L. Papadimitriou, Mat. Sci. Engin. B 176 (2011) 512.
[54] P. Heitjans, M. Masoud, A. Feldhoff, M. Wilkening, Faraday Discuss. 134 (2007) 67.
[55] Rahn, J.; Hüger, E.; Dörrer, L.; Ruprecht, B.; Heitjans, P.; Schmidt, H.; Self-Diffusion of Lithium in Amorphous Lithium Niobate Layers, Z. Phys. Chem. 226 (2012) 439.
[56] J. Rahn, E. Hüger, L. Dörrer, B. Ruprecht, P. Heitjans, H. Schmidt, Defect and Diffusion Forum 323-325 (2012) 69.
[60] B. Reichmann, A. J. Bard, J. Electrochem. Soc. 128 (1981) 344.

[61] F. Lüdtke, K. Buse, and B. Sturman, Phys. Rev. Lett. 109 (2012) 026603.
[62] E. Hüger, J. Rahn, J. Stahn, Th. Geue, P. Heitjans, H. Schmidt, Phys. Chem. Chem. Phys. 16 (2014) 3670.
[63] A. V. Chadwick, S. L. P. Savin, Solid State Ionics 177 (2006) 3001.
[64] Kamaya, N.; Homma, K.; Yamakawa, Y.; Hirayama, M.; Kanno, R.; Yonemura, M.; Kamiyama, T.; Kato, Y.; Hama, S.; Kawamoto, K.; Mitsui, A.; A lithium superionic conductor, *Nature materials* 10 (2011) 682.
[65] M. Ogawa, R. Kanda, K. Yoshida, T. Uemura, K. Harada, J. Power Sources 205 (2012) 487.
[66] N. Ohta, K. Takada, I. Sakaguchi, L. Zhang, R. Ma, K. Fukuda, M. Osada, and T. Sasaki, Electrochem. Commun. 9 (2007) 1486.
[67] M. Schmitt, S. Heusing, M. A. Aegerter, A. Pawlicke, C. Avellaneda, Solar Energy Materials and Solar Cells 54 (1998) 9.
[68] J.-T. Han, D.-Q. Liu, S.-H. Song, Y. Kim, J. B. Goodenough, Chem. Mater. 21 (2009) 4753.
[69] Z. Zhu, A. Kushima, Z. Yin, L. Qi, K. Amine, J. Lu, J. Li, Nature Energy 1 (2016) 16111.
[70] E. Hüger, and K. Osuch, Eur. Phys. J. B 37 (2004) 149.
[71] F.A.Ma'Mari, T. Moorsom, G. Teobaldi, W. Deacon, Th. Prokscha, H. Luetkens, S. Lee, G.E. Sterbinsky, D. A., Arena, D. A. MacLaren, M. Flokstra, M. Ali, M. C. Wheeler, G. Burnell, B. J. Hickey, O. Cespedes, Nature 524 (2015) 69.
[72] E. Hüger, and K. Osuch, Europhys. Lett. 63 (2003) 90.
[p181] E. Hüger, and K. Osuch, Solid State Commun. 131 (2004) 175.
[74] E. Hüger, and K. Osuch, Eur. Phys. J. B 44 (2004) 145.
[75] E. Hüger, and K. Osuch, Phys. Rev. B. 72 (2005) 085432.
[76] T. Kana, E. Hüger, D. Legut, M. Cak, and M. Sob, Phys. Rev. B. 93 (2016) 134422.
[77] C. P. Kwan, R. Chen, U. Singisetti, and J. P. Bird, Appl. Phys. Lett. 106 (2015) 112901.
[78] P. Borisov, T. Ashida, T. Nozaki, M. Sahashi, and D. Lederman, Phys. Rev. B 93 (2016) 174415.
[79] H.Y. Hwang, S.-W. Cheong, Science 278 (1997) 1607.
[80] L. Fallorino, Ch. Binek, A. Berger, Phys. Rev. B 91 (2015) 214403.
[81] M. Schneider, H. Möhwald, S. Akarib, The Journal of Adhesion 79 (2003) 597.
[82] Vancea et al. Surface Science 218 (1989) 108.
[83] N. Münzenrieder, Ch. Zysset, L. Petti, Th. Kinkeldei, G.A. Salvatore, G. Tröster, Solid-State Electronics 84 (2013) 198.
[84] L. Petti, N. Münzenrieder, Ch. Vogt, H. Faber, L. Büthe, G. Cantarella, F. Bottacchi, Th. D. Anthopoulos, G. Tröster, Appl. Phys. Rev. 3 (2016) 021303.
[85] D. Grimm, C.C.B. Bufon, Ch. Deneke, P. Atkinson, D.J. Thurmer, F. Schäffel, S. Gorantla, A. Bachmatiuk, O. G. Schmidt, Nano Lett. 13 (2013) 213.
[86] Y. Yang, G. Ruan, Ch. Xiang, G. Wang, J.M. Tour, J. Am. Chem. Soc. 136 (2014) 6187.
[87] G. X. Feng, L. F. Li, J. Y. Liu, N. Liu, H. Li, X. Q. Huang, L. Q. Chen, K. W. Nam, W. S. Yoon, J. Mater. Chem. 19 (2009) 2993.
[88] Y. Lyu, L. Ben, Y. Sun, D. Tang, K. Xu, L. Gu, R. Xiao, H. Li, L. Chen, X. Huang, J. Power Sources 273 (2015) 1218.
[89] E. Hüger, L. Dörrer, J. Rahn, T. Panzner, J. Stahn, G. Lilienkamp and H. Schmidt, *Nano Lett.*, **13**, 1237 (2013).
[90] H. Kiesig, *Annalen der Physik*, 402 (1931) 769.
[91] V. Holy, U. Pietsch and T. Baumbach, *High-resolution X-ray scattering from thin films and multilayers*, Springer, Berlin, Heidelberg, New York, (1999). ISBN 3-540-62029-X.
[92] C. Braun, Parratt32 or the reflectometry tool, HMI, Berlin, [http://www.helmholtz-berlin.de].
[93] See [http://www.ncnrs.nist.gov/resources/sldcalc.html].
[94] B. Jerliu, L. Dörrer, E. Hüger, G. Borchardt, R. Steitz, U. Geckle, V. Oberst, M. Bruns, O. Schneider and H. Schmidt, *Phys. Chem. Chem. Phys.*, **15**, 7777 (2013).
[95] P. Villars, Material Phases Data System (MPDS), CH-6354 Vitznau, Switzerland; Springer Materials; sd_0314160 (Springer-Verlag GmbH, Heidelberg, 2014), http://materials.springer.com/isp/crystallographic/docs/sd_0314160 accessed: 07-09-2015
[96] U. Welzel, J. Ligot, P. Lamparter, A. C. Vermeulen, E. J. Mittemeijer, J. Appl. Cryst. 38 (2005) 1.
[97] H. Nörenberg, H.-G. Neumann, Thin Solid Films 198 (1991) 241.
[98] K. Khojier, H. Savaloni, Z. Ashkabusi, N. Z. Dehnavi, Appl. Surf. Sci. 284 (2013) 489.
[99] J. Lin, I. Dahan, Surf. Coat. Technol. 265 (2015) 154.
[100] M. M. Abdullah, F. M. Rajab, and S. M. Al-Abbas, AIP Advances 4 (2014) 027121.
[101] S.-H. Shim, Th. S. Duffy, R. Jeanloz, C.-S. Yoo and V. Iota, Phys. Rev. B 69 (2004) 144107.
[102] P.M. Sousa, A. J. Silvestre, and O. Conde, Thin Solid Films 519 (2011) 3653.
[103] F. Wang, W. Li, M. Hou, C. Li, Y. Wang, and Y. Xia, J. Mater. Chem. A 3 (2015) 1703.
[104] G. Carta, M. Natali, G. Rossetto, P. Zanellla, G. Salmaso, S. Restello, V. Rigato, S. Kaciulis, and A. Mezzi, Chem. Vap. Deposition 11 (2005) 375.
[105] Y. Murakami, A. Sawata, and Y. Tsuru, J. Mater. Sci. 34 (1999) 951.
[106] O. Monnereau, L. Tortet, C.E.A. Grigorescu, D. Savastru, C. R. Iordanescu, F. Guinneton, R. Notonier, A. Tonetto, T. Zhang, I.N. Mihailescu, D. Stanoi, and H.J. Trodahl, Journal of Optoelectronics and Advanced Materials, 12 (2010) 1752.
[107] T. Ivanova, K. Gesheva, A. Cziraki, A. Szekeres, and E. Vlaikova, J. Phys.: Conf. Series 113 (2008) 012030.
[108] H. Schmidt, G. Borchardt, A. Müller, J. Bill, J. Non-Cryst. Sol. 341 (2004) 133.
[109] S. K. Soni, B. W. Sheldon, X. Xiao, A. Tokranov, Scripta Materialia **64** (2011) 307.
[p110] K. Zhao, G. A. Tritsaris, M. Pharr, W. L. Wang, O. Okeke, Z. Suo, J. L. Vlassak, E. Kaxiras, Nano Lett. **12** (2012) 4397.
[111] S. K. Soni, B. W. Sheldon, X. Xiao, A. F. Bower, M. W. Verbrugge, J. Electrochem. Soc. **159** (2012) A1520.
[112] P. Liu, N. Sridhar, Y.-W. Zhang, J. Appl. Phys. **112** (2012) 093507.
[113] Y. F. Gao, M. Zhou, J. Appl. Phys. **109** (2011) 014310.
[114] Y. F. Gao, M. Cho, M. Zhou, J. Mech. Phys. Solids **61** (2013) 579.
[115] L. Brassart, K. Zhao, Z. Suo, Int. J. Solids Struct. **50** (2013) 1120.
[116] L. Brassart, Z. Suo, J. Mech. Phys. Solids **61** (2013) 61.
[117] M. T. McDowell, S. Xia, T. Zhu, Extreme Mechanics Letters (2016) http://dx.doi.org/10.1016/j.eml.2016.03.004
[118] W. Gruber, C. Baehtz, M. Horisberger, I. Ratschinski, H. Schmidt, Appl. Surf. Sci. 368 (2016) 341.
[119] G. Calvarin, A. M. Huntz, A. Hugot Le Goff, S. Joiret, and M.C. Bernard, Scripta Materialia 38 (1998) 1649.
[120] J. Mougin, T. Le Bihan, and G. Lucazeau, Journal of Physics and Chemistry of Solids 62 (2001) 553.
[121] M. Kemdehoundja, J. L. Grosseau-Poussard, and J. F. Dinhut, Appl. Surf. Sci. 256 (2010) 2719.

[122] Bruker Optics Inc., USA, Application Note 520: Contactless characterization of amorphous and microcrystalline silicon using Raman micro spectroscopy. https://www.bruker.com/fileadmin/user_upload/8-PDF Docs/OpticalSpectrospcopy/Raman/SENTERRA/AN/AN520_amorphous-microcrystal-silicon_EN.pdf
[123] P. Shearing, Y. Wu, S. J. Harris, N. Brandon, Interface, fall (2011) 53.
[124] B. M. Weckhuysen, R. A. Schoonheydt, J.-M. Jehng, I. E. Wachs, S. J. Cho, R. Ryoo, S. Kijistra, E. Poels, J. Chem. Soc. Faraday Trans. 91 (1995) 3245.
[125] S. M. K. Airaksinen, A. O. I. Krause, J. Sainio, J. Lahtinen, K.-J. Chao, M. O. Guerrero-Perez, M. A. Banares, Phys. Chem. Chem. Phys. 5 (2003) 4371.
[126] G. Corradi, A.V. Chadwick, A. R. West K. Cruickshank, M. Paul, Radiation Effects and Defects in Solids 134 (1995) 219.
[127] A. G. McKale, B. W. Vea, A. P. Paulikas, S.-K. Chan, and G. S. Knapp., J. Am. Chem. Soc. 110 (1988) 3763.
[128] P. J. Schilling, J.-H. He, E. Ma, J. Phys. IV France 7 (1997) C2-1221.
[129] T. Miyanga, K. Takasugi, T. Ohba, T. Aida, T. Okazaki, J. Physics: Conf. Series 502 (2014) 012032.
[130] Y. Babanov, S. Kiryanov, A. Siderenko, L. Romashev, D. Vyalikh, S. Molodstov, G. Guentherodt, U. Ruediger, Y. Dedkov, M. Fonine, K. Baberschke, H. Wende, Y. U. Idzerda, Physica Scripta T115 (2005) 194.
[131] Md. Ahamad Mohiddon, K. Lakshun Naidu, M. Ghanashyam Krishna, G. Dalba, S. I. Ahmed, and F. Rocca, J. Appl. Phys. 115 (2014) 044315.
[132] Weine Olovsson, Björn Alling, and Martin Magnuson, J. Phys. Chem. C 120 (2016) 12890.
[133] H. Schmidt, W. Gruber, T. Gutberlet, M. Ay, J. Stahn, U. Geckle and M. Bruns, J. Appl. Phys., 102 (2007) 043516.
[134] S. Chakravarty, U. Tietze, D. Lott, N. P. Lalla, A. Gupta and H. Schmidt, Phys. Rev. B 80 (2009) 014111.
[135] S. Chakravarty, M. Jiang, H. Schmidt, U. Tietze, D. Lott, T. Geue and J. Stahn, Acta Mater. 59 (2011) 5568.
[136] F. Strauß, B. Jerliu, T. Geue, J. Stahn and H. Schmidt, J. Appl. Phys. 119 (2016) 175102.
[137] R. Singh, J. Magn. Magn. Mater., 346 (2013) 58.
[138] Z. Wang, Z. Li, and Y. Q. Fu, ChemElectroChem, 4 (2017) 1523.
[139] Z. Wang, ACS Appl. Mater. Interfaces, 9 (2017) 15893.
[140] J. Maier, Nature Mater., 4 (2005) 805.
[141] L. A. Haverkate, W. K. Chan and F. M. Mulder, Adv. Funct. Mater., 20 (2010) 4107.
[142] R. O. Dillon, J. A. Woollam, and V. Katkanant, Phys. Rev. B, 29 (1984) 3482.
[143] M. A. Tamor, and W. C. Vassell, Journal of Applied Physics, 76 (1994) 3823; doi: 10.1063/1.357385
[144] A. C. Ferrari, and J. Robertson, Phys. Rev. B, 61 (2000) 14095.
[145] A. C. Ferrari, Solid State Communications 143 (2007) 47.
[146] Liping Wang, Renhui Zhang, Ulf Jansson, and Nils Nedfors, Scientific Reports, 5 (2015) 11119; doi: 10.1038/srep11119